

Evaluation of New Submillimeter VLBI Sites for the Event Horizon Telescope

Alexander W. Raymond ¹, Daniel Palumbo ^{1,2}, Scott N. Paine ¹, Lindy Blackburn ^{1,2}, Rodrigo Córdova Rosado ^{1,3}, Sheperd S. Doeleman ^{1,2}, Joseph R. Farah ^{1,4}, Michael D. Johnson ^{1,2}, Freek Roelofs ⁵, Remo P. J. Tilanus ⁶, and Jonathan Weintroub ^{1,2}

¹ Center for Astrophysics | Harvard & Smithsonian, 60 Garden Street, Cambridge, MA 02138, USA; alexander.raymond@cfa.harvard.edu

² Black Hole Initiative, Harvard University, 20 Garden Street, Cambridge, MA 02138, USA

Department of Astrophysical Sciences, Princeton University, 4 Ivy Lane, Princeton, NJ 08544, USA

Department of Astrophysical Sciences, Princeton University, 4 by Lane, Princeton, NJ 06344, USA

4 University of Massachusetts Boston, 100 William T. Morrissey Boulevard, Boston, MA 02125, USA

Abstract

The Event Horizon Telescope (EHT) is a very long-baseline interferometer built to image supermassive black holes on event-horizon scales. In this paper, we investigate candidate sites for an expanded EHT array with improved imaging capabilities. We use historical meteorology and radiative transfer analysis to evaluate site performance. Most of the existing sites in the EHT array have median zenith opacity less than 0.2 at 230 GHz during the March/April observing season. Seven of the existing EHT sites have 345 GHz opacity less than 0.5 during observing months. Out of more than 40 candidate new locations analyzed, approximately half have 230 GHz opacity comparable to the existing EHT sites, and at least 17 of the candidate sites would be comparably good for 345 GHz observing. A group of new sites with favorable transmittance and geographic placement leads to greatly enhanced imaging and science on horizon scales.

Unified Astronomy Thesaurus concepts: Very long baseline interferometry (1769); Submillimeter astronomy (1647); Black holes (162); Radio observatories (1350); Atmospheric effects (113)

1. Introduction

The Event Horizon Telescope (EHT) is a very long-baseline interferometry (VLBI) array operating at 230 GHz (Doeleman et al. 2009; Event Horizon Telescope Collaboration et al. 2019a). In 2017, eight telescopes at six sites participated in the EHT observing campaign that yielded the first horizon-scale images of the supermassive black hole in the M87 galaxy (or M87*; Event Horizon Telescope Collaboration et al. 2019b). The planned 2021 EHT array includes 10 telescopes at nine sites plus the Atacama Large Millimeter/submillimeter Array (ALMA): the Atacama Pathfinder Experiment (APEX), the Greenland Telescope (GLT), the Instituto de Radioastronomía Milimétrica 30 m telescope (IRAM-30 m), the James Clerk Maxwell Telescope (JCMT), the 12 m radio telescope at Kitt Peak (KP) operated by the University of Arizona, the Large Millimeter Telescope Alfonso Serrano (LMT), the Northern Extended Millimeter Array (NOEMA), the Submillimeter Array (SMA), the Submillimeter Telescope (SMT), and the South Pole Telescope (SPT). The coordinates for these stations are listed in Table 1. Generally, these stations were developed as standalone submillimeter facilities and perform non-VLBI observations throughout most of the year.

There is an active effort (Blackburn et al. 2020) to expand the array to new sites and higher frequency (e.g., 345 GHz), which will improve imaging and modeling of M87* and the other primary science target, Sgr A*, the black hole candidate at the center of the Milky Way (Doeleman et al. 2008). These improvements will lead to a new instrument, the next-generation EHT (ngEHT), that is designed to deliver

transformative science capabilities. In this paper, we identify a set of candidate ngEHT sites, characterize their meteorological suitability for 230 and 345 GHz observations, and evaluate the additional VLBI baseline coverage they provide beyond the existing EHT array. New analysis for the existing EHT sites is also presented.

There are many factors to consider in the selection of new sites for ngEHT stations. The elevation of the primary science targets above the horizon, mutual visibility of those sources with the existing sites in the array, and the incremental Fourier coverage contributed by a new site are all key considerations. New Fourier coverage improves the VLBI instrument in several ways. Dense sampling improves imaging fidelity, and baseline redundancy in dense arrays is a powerful tool for calibration (Pearson & Readhead 1984). A sufficiently dense array may even allow imaging to rely on calibration-independent closure quantities (three- and four-station products) instead of visibilities (two-station products; Chael et al. 2018; Blackburn et al. 2019). Finally, an array producing dense sampling is robust against losing one or two stations because of poor weather on a particular day.

The meteorological conditions are a key consideration in the evaluation of a new site. Water is the atmospheric constituent that primarily governs atmospheric transmission and brightness temperature at millimeter and submillimeter wavelengths. We characterize precipitable water vapor (PWV, expressed in millimeter units) and liquid water path (LWP, expressed in microns) in our analysis. Although submillimeter site evaluations usually emphasize the importance of PWV statistics, clouds consisting of liquid water droplets can also contribute significantly to opacity (Matsushita & Matsuo 2003). Analysis of EHT data indicates that the imaging capability of the ngEHT will depend primarily on increasing the number of VLBI

Department of Astrophysics, Institute for Mathematics, Astrophysics and Particle Physics (IMAPP), Radboud University, P.O. Box 9010, 6500 GL Nijmegen, The Netherlands

⁶ Department of Astronomy and Steward Observatory, University of Arizona, 933 N. Cherry Avenue, Tucson, AZ 85721, USA Received 2020 July 6; revised 2020 October 2; accepted 2020 October 20; published 2021 February 16

⁷ This black hole is also named $P\bar{o}wehi$ by A Hui He Inoa (Kimura et al. 2019).

Table 1
Locations of Existing Sites (2021) in the Event Horizon Telescope
Array (Event Horizon Telescope Collaboration et al. 2019a)

Site	Location (Region, Country)	Lat.	Lon.	Alt. (m)	
ALMA	Antofagasta, CL	-23.03	-67.75	5070	
APEX	Antofagasta, CL	-23.01	-67.76	5100	
GLT ^a	Avannaata, GL	76.54	-68.69	90	
IRAM-30 m	Granada, ES	37.07	-3.39	2920	
JCMT	Hawaii, US	19.82	-155.48	4120	
KP	Arizona, US	31.96	-111.61	1900	
LMT	Puebla, MX	18.98	-97.31	4600	
NOEMA	PrAlpes-Côte				
	d'Azur, FR	44.63	5.91	2620	
SMA	Hawaii, US	19.82	-155.48	4110	
SMT	Arizona, US	32.70	-109.89	3160	
SPT ^b	South Pole, Antarctica	-90.00	45.00	2820	

Notes.

baselines, and only secondarily on sensitivity, so lower altitude sites with variable atmospheric conditions will be considered viable. Our interest in sites that achieve good Fourier coverage motivates our analysis of meteorological conditions at suboptimal places, and distinguishes the present study from previous submillimeter site surveys, e.g., Tremblin et al. (2012).

Historically, EHT observations have been scheduled for March or April. Our analysis specifically addresses observing conditions during those months, which are the time of year when the sources are above the horizon at nighttime (the time of day when observing conditions are generally best for most sites), and when PWV paths are favorable across the Northern and Southern Hemispheres.

There are relatively few undeveloped locations for new telescopes in dry places that provide new VLBI baselines of hundreds to thousands of kilometers, which is the station spacing required to fill gaps in the existing EHT coverage. To illustrate this point, we divide the globe into 1° latitude by 1° longitude squares, and within each square, the PWV and LWP values are calculated for the location of the highest peak based on the Modern-Era Retrospective analysis for Research and Applications, version 2 (MERRA-2; Gelaro et al. 2017). In Figure 1, peaks are highlighted between 60° latitudes that have median PWV and LWP values less than 5 mm and 5 μ m, respectively. The locations of the dry peaks agree with previous PWV maps, e.g., Suen et al. (2015), which have shown that the driest places tend to be nonequatorial high planes. Maunakea, Parque Nacional Pico de Orizaba, the Atacama Desert, and other places hosting existing submillimeter telescopes emerge on the plot. The Himalayas, Alps, Andes, and southwest United States each have many low-PWV sites. The latter three regions have sustained covisibility of the primary science targets with ALMA, which is the most sensitive submillimeter station. The large signal-to-noise ratio (S/N) achieved on ALMA baselines enables the atmospheric phase correction that improves and calibrates detections on non-ALMA baselines (Event Horizon Telescope Collaboration et al. 2019c). Selecting sites that have covisibility with the existing EHT stations also capitalizes on the N(N-1)/2 growth in the number of baselines, where N is

the number of stations that can simultaneously observe a given source.

Using the PWV map as a guide together with knowledge about existing infrastructure and previous astronomical site evaluations, e.g., Suen et al. (2014), we identify 45 sites to study in detail. Those sites are plotted in Figure 2 and their longitude, latitude, and altitude coordinates are listed in Table 2. The capitalized site identifiers defined in this table are used throughout the text. These sites cover a broad sampling of longitudes and latitudes, regions, and climates. Our main objective in this paper is to catalog potential sites based primarily on weather and Fourier coverage. The analysis we present is an initial step toward array expansion. Many of the places we analyze already host an observatory or existing roads and infrastructure; however, some of the sites we present are remote and would require responsible assessments of the environmental and cultural impact of new construction to determine if development is viable.8

We perform a radiative transfer analysis of the sites using historical meteorological statistics. From that analysis, we present transmittances at 230 GHz and higher frequencies up to 500 GHz. Observations at 345 GHz are of particular interest as a way to improve angular resolution and reduce scattering by the interstellar medium on the line of sight to Sgr A*. In general, 345 GHz observations demand sites with better weather than sites that are suitable for 230 GHz observations. Our calculations show which sites, new and existing, are feasible for high-frequency observing.

We evaluate the Fourier coverage contributed by the candidate stations in a few ways. First, we present the geometric Fourier coverage contributed by each station while paying particular attention to the baselines with ALMA. Second, we use the meteorological statistics for each site to calculate the probabilistic Fourier coverage from a set of Monte Carlo observing trials. Finally, we perform test imaging reconstructions of M87* and Sgr A* simulations to illustrate how new stations would enhance the imaging performance of the EHT. We find that a collection of sites chosen for their favorable probabilistic Fourier coverage and good conditions is able to significantly improve the fidelity of the reconstructions.

2. Methods

We use atmospheric state data from MERRA-2 as inputs to our calculations. Each site is analyzed using a 10 year historical data set ending on 2019 January 1. The data sets consist of 3 hr averages, gridded to 0°.5 latitude and 0°.625 longitude, and 42 vertical pressure levels. Each time, position, and altitude datum contains the state of the atmosphere including water quantities (vapor, liquid, and ice) and temperature. The gridded data are interpolated to the precise location of a candidate site. We calculate water statistics as well as submillimeter radiative properties with the aid of the *am* atmospheric modeling and radiative transfer code (Paine 2019). For each site, we compute 10 year monthly statistics of column-integrated water vapor and liquid clouds, and we use those to calculate the spectral

^a site cannot observe Sgr A*.

b site cannot observe M87*.

⁸ The FUJI, KEN, and KILI sites we analyze in this study are UNESCO World Heritage Sites. In each case the site has either been previously considered or used for astronomical purposes (Sekimoto et al. 2000; Graham et al. 2016). At the KILI site there are local efforts to explore the location for possible astronomical research (Dr. Noorali T. Jiwaji, private communication). We present these sites to assess their meteorological viability but acknowledge that considerations beyond just the scientific suitability will determine the future possibilities for ngEHT telescopes at these locations.

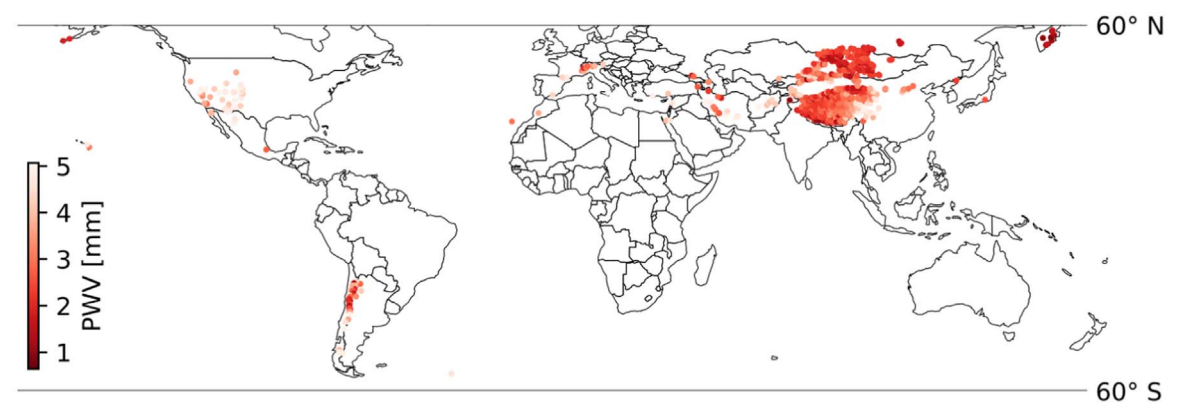


Figure 1. Worldwide March PWV for peaks above 2000 m in each 1° latitude/longitude square between 60° S and 60° N latitude. MERRA-2 data sets for years 2009 through 2012 were averaged. A cutoff of 5 mm is applied.

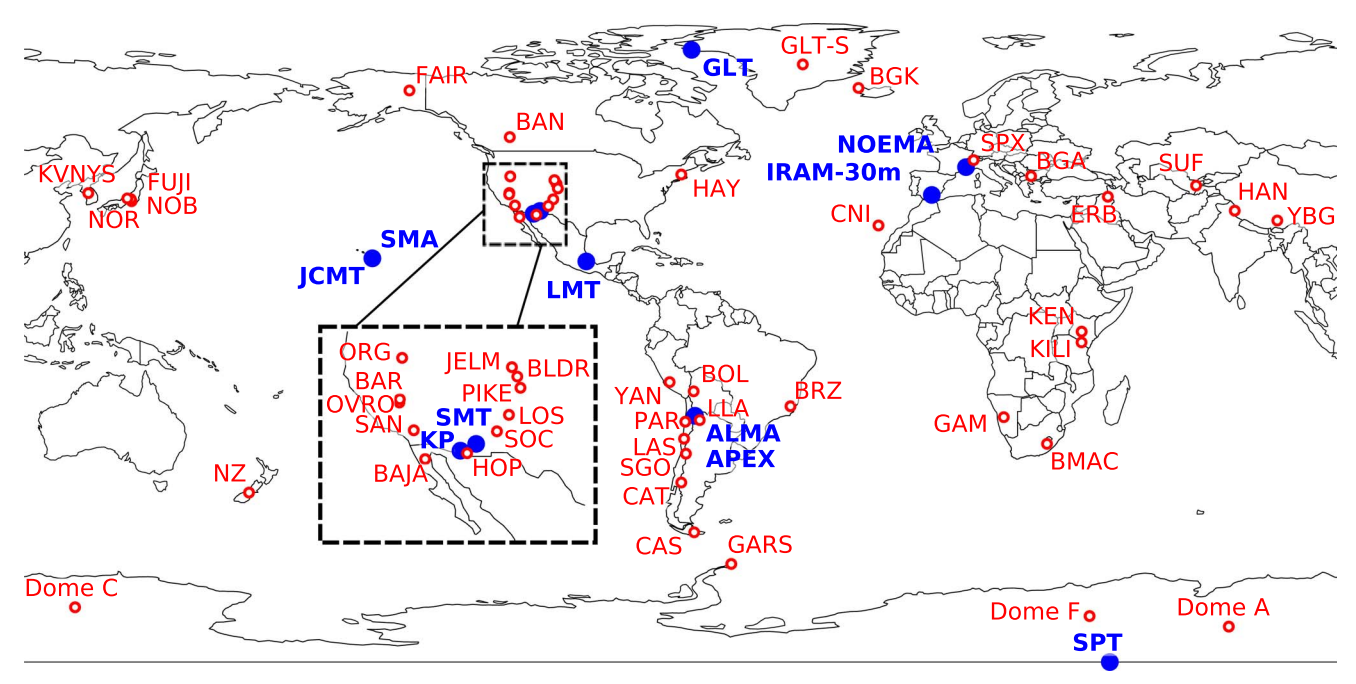


Figure 2. Map of planned 2021 EHT sites (blue, bold) listed in Table 1 and 45 potential new sites (red) for the ngEHT listed in Table 2. The map is centered on the 2021 EHT sites.

opacity $\tau(\nu)$ and brightness temperature $T_{\rm b}$ as a function of frequency ν following the methodology described in Paine (2018, 2019). The liquid and ice opacity calculations utilize the Rayleigh approximation.

Submillimeter wavelength observations are affected by meteorology in several ways, and we consider various factors in our site evaluation. First, PWV statistics are frequently used as proxies for submillimeter observing conditions, and we present monthly PWV statistics for both existing EHT and candidate ngEHT sites. The LWP statistic is another important metric we consider. The LWP contribution to zenith opacity will be approximately 2.5×10^{-3} and $3.5 \times 10^{-3} \, \mu\text{m}^{-1}$ at 230 and 345 GHz, respectively, with weak temperature dependence (Paine 2019). In other words, 100 μ m of LWP contributes 0.25 to the opacity at 230 GHz. Figure 3 shows the effective system temperature (defined later in this section) at a typical lower bound on the telescope elevation angle during VLBI observations; at $100 \,\mu\mathrm{m}$ LWP column, liquid clouds become the dominant source of system noise. Consequently, we include the effects of all water phases in our radiative transfer analysis.

An additional metric that is important in interferometry is the coherence time of the atmosphere. Turbulence cells in the moist atmosphere cause phase fluctuations in the interferometric response of a VLBI baseline resulting in signal loss for extended coherent integrations. Here, we define the coherence time to be the integration interval beyond which the VLBI signal loss rises above 10%. During the 2017 EHT observations, the coherence time was typically in the range of 10-20 s on ALMA baselines (Event Horizon Telescope Collaboration et al. 2019a). Strong S/N detections to ALMA are used to correct the phase data and enable longer coherent integration time. The spatiotemporal grid for MERRA-2 is not suitably fine for calculating coherence times, so we do not consider that effect in this analysis; however, atmospheres with small PWV and LWP characteristics will generally have small wet path delays and consequently better coherence times (Thompson et al. 2017).

We calculate the incremental Fourier coverage, or Fourier filling, of the M87* and Sgr A* sources for new sites compared to a fiducial array, i.e., the 2021 EHT array. As Earth rotates

 Table 2

 Next-generation Event Horizon Telescope Candidate Sites

Site	Location (Region, Country)	Lat. (°)	Lon. (°)	Alt. (m)	
BAJA	Baja California, MX	31	-115	2500	
BAN ^a	Alberta, CA	53	-118	2000	
BAR	California, US	38	-118	3500	
BGA	Sofia, BG	42	24	2500	
BGK ^a	Westfjords, IS	66	-23	500	
BLDR	Colorado, US	40	-105	2500	
BMAC	Eastern Cape, ZA	-31	28	2500	
BOL	La Paz, BO	-16	-68	5000	
BRZ	Espírito Santo, BR	-20	-42	2500	
CAS	Tierra del Fuego, AR	-55	-68	500	
CAT	Río Negro, AR	-33	-71	2000	
CNI	La Palma, ES-CN	29	-71 -18	2000	
Dome Ab	Antarctica	-80	-18 77	4000	
Dome C ^b	Antarctica	-80 -75	123	3000	
Dome F ^b	Antarctica	-73 -78	39	3500	
ERB	Kurdistan, IQ	-78 37	39 44	2000	
FAIR ^a					
	Alaska, US	65	-145	1000	
FUJI	Fujinomiya &	25	120	2500	
CAM	Yamanashi, JP	35	139	3500	
GAM	Khomas, NA	-23	16	2000	
GARS	Antarctica	-63	-58	0	
GLT-S ^a	Northeastern, GL	73	-38	3000	
HAN	Jammu & Kashmir, IN	33	79	4000	
HAY	Massachusetts, US	43	-71	0	
HOP	Arizona, US	32	-111	2000	
JELM	Wyoming, US	41	-106	2500	
KEN	Meru, KE	-0	37	4000	
KILI	Kilimanjaro, TZ	-3	37	4500	
KVNYS	Seoul, KR	38	127	0	
LAS	Coquimbo, CL	-29	-71	2000	
LLA	Salta, AR	-24	-66	4500	
LOS	New Mexico, US	36	-106	2000	
NOB	Nagano, JP	36	138	1000	
NOR	Gifu, JP	36	138	2500	
NZ	Canterbury, NZ	-44	171	2000	
ORG	Oregon, US	42	-118	2000	
OVRO	California, US	37	-118	1000	
PAR	Antofagasta, CL	-25	-70	2500	
PIKE	Colorado, US	39	-105	4000	
SAN	California, US	34	-117	2500	
SGO	Santiago, CL	-33	-70	3500	
SOC	New Mexico, US	34	-108	2000	
SPX	Bern, CH	47	8	3500	
SUF	Jizzakh, UZ	40	68	2000	
YAN	Huanca Sancos, PE	-14	-75	4500	
YBG	Yangbajing Tibet, CN	30	91	4000	

Notes.

during an observation, each baseline samples a set of Fourier components that traces tracks in the u-v (east—west and north—south) Fourier plane. The incremental Fourier coverage is the fractional increase in the u-v area sampled by an additional station compared to the fiducial array. The width of each track is given by 0.71 divided by the field of view (FoV) adopted for imaging, which corresponds to the half-width of the visibility response to a filled disk occupying the FoV on the sky (Palumbo et al. 2019). If a new site primarily samples Fourier

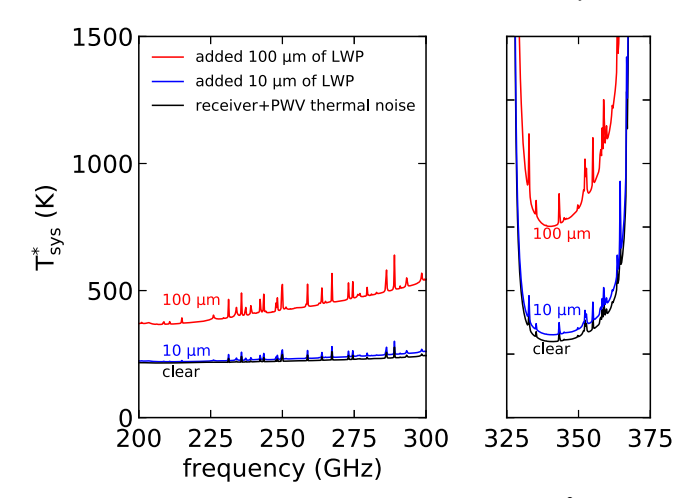


Figure 3. Effective system temperature along a line of sight at 20° elevation for the ALMA/APEX site. The indicated LWP is added to the meteorological conditions of the April clear-sky days (i.e., to the days with less than $10~\mu m$ LWP) at the 450 mbar pressure level. The liquid component can double the effective system temperatures at 230 or 345 GHz.

space that is already covered by existing baselines, then its incremental coverage is small. If a new site samples spatial frequencies that are not covered by the existing array, then its incremental coverage will be large. There are plans to position an antenna at the Greenland Summit, which has excellent atmospheric conditions (Matsushita et al. 2017). We assume that the GLT site remains in the fiducial array and evaluate the incremental addition of a GLT-S station.

To incorporate the effects of weather in the Fourier filling metric, we perform 45 repeated Monte Carlo trial simulations of the weather-dependent observations using eht-imaging (Chael et al. 2016, 2018) based on the statistical distribution of opacity. In each trial, we flag low S/N portions of the Fourier coverage (S/N < 3), in accordance with longbaseline scans reported in Event Horizon Telescope Collaboration et al. 2019c), and report the average coverage across all trials. We make some simplifying assumptions like neglecting losses resulting from the beam pointing off source or mechanical defocusing. Those effects could be incorporated in the future using synthetic data tools developed for the EHT (Roelofs et al. 2020). The M87* source model we use in the simulations has 0.6 Jy flux density at 230 GHz on the spatial scale of the event horizon. A scattering kernel is applied to the Sgr A* source model to simulate the effects of the interstellar medium (Johnson et al. 2018), and a short baseline 230 GHz flux density of 2.3 Jy is used for that source.

The simulated S/N values for each synthetic observation are governed by the system-equivalent flux density for each site $(SEFD_i)$,

$$SEFD_i = 2kT_{\text{sys},i}^* / A_{\text{eff},i}, \tag{1}$$

where $A_{\text{eff},i}$ is the effective antenna area and k is the Boltzmann constant. For the 2021 array as well as the new sites HAY, KVNYS, LAS, NOB, SUF, and GAM, we base the collecting area on the antenna diameter of the existing or planned telescopes, which are 37 (Rogers et al. 1993; Usoff et al. 2014), 21 (Lee et al. 2011), 15 (Booth et al. 1989), 45 (Ishiguro et al. 1986), 70, and 15 m, respectively. For all other sites, we assume a 10 m diameter

^a site cannot observe Sgr A*.

b site cannot observe M87*.

antenna. Known aperture efficiencies are used, and for the new 10 m stations we assume a Ruze-formula (Thompson et al. 2017) aperture efficiency based on a 64 μ m rms surface accuracy, which is the quadrature sum of a 40 μ m primary surface accuracy and an effective 50 μ m focus offset. The SEFD $_i$ values depend on the effective system temperature, $T_{\rm sys,i}^* = [T_{\rm R} + T_{\rm b,i}(\theta)]e^{\tau_i(\theta)}$ (Thompson et al. 2017), and the opacity for a given site. $\tau_i(\theta)$ is the opacity toward the source as a function of elevation, θ , where a lower limit of 10° in elevation is applied.

We adopt a receiver temperature, $T_{\rm R}$, of 60 and 100 K for all sites at 230 and 345 GHz, respectively, and use the interquartile ranges for sky-brightness temperature ($T_{\rm b,i}$) and opacity (τ_i) to generate a Gaussian random variable for $T_{\rm sys,i}^*$. The random variables at the ALMA/APEX, JCMT/SMA, and KP/SMT EHT sites are assumed to be correlated while those for candidate ngEHT sites are assumed to be uncorrelated. The S/N of the visibility measured on a single baseline is (Thompson et al. 2017)

$$S/N = \eta S_{\nu}(\vec{u}) \sqrt{\frac{2\Delta\nu\tau_{c}}{SEFD_{1}SEFD_{2}}},$$
 (2)

where η is the digital and processing efficiency, $S_{\nu}(\vec{u})$ is the correlated flux density on baseline \vec{u} , $\Delta \nu$ is the bandwidth, and $\tau_{\rm c}$ is the integration time. We specify integration times of 300 s (M87*) or 100 s (Sgr A*, shorter than the smallest expected period of the innermost stable circular orbit). The bandwidth specified for S/N calculations is 2 (as for the current EHT) or 8 GHz (ngEHT), and corresponds to the Nyquist band of a single digitizer (Event Horizon Telescope Collaboration et al. 2019a). We call this the fringe-finding bandwidth. Multiple fringe-finding sidebands are aggregated for imaging: two of 2 GHz each in 2017, four of 2 GHz each in 2021, and two of 8 GHz each for the ngEHT. Those correspond to a total bandwidth across two polarizations of 8, 16, and 64 GHz in the respective years (assuming simultaneous dual-frequency 230+345 GHz observing with the ngEHT). The dual-frequency approach increases the Fourier coverage, and with the appropriate model, the two frequencies can be combined to synthesize a single image (Sault & Wieringa 1994). We account for the slightly different center frequencies of each sideband when calculating the Fourier filling.

Finally, we perform imaging reconstructions of M87* and Sgr A* using a possible ngEHT array chosen by picking from among the best sites from the Fourier filling metric. The reconstruction is meant as an example of how new sites will affect the imaging capabilities of the EHT instrument. The source models for those reconstructions are general-relativistic magnetohydrodynamic (GRMHD) simulations of accretion flows (Rowan et al. 2017; Chael et al. 2018, 2019). We calculate the noise for each baseline in the same manner described above under median opacity conditions. For M87*, we generate synthetic data with a 40% duty cycle, and for Sgr A*, we use a brief 100 s snapshot observation that begins at a time of day when the Fourier filing is greatest, which can be different for different arrays. We apply an imaging process similar to the published eht-imaging script released alongside Event Horizon Telescope Collaboration et al. (2019d).

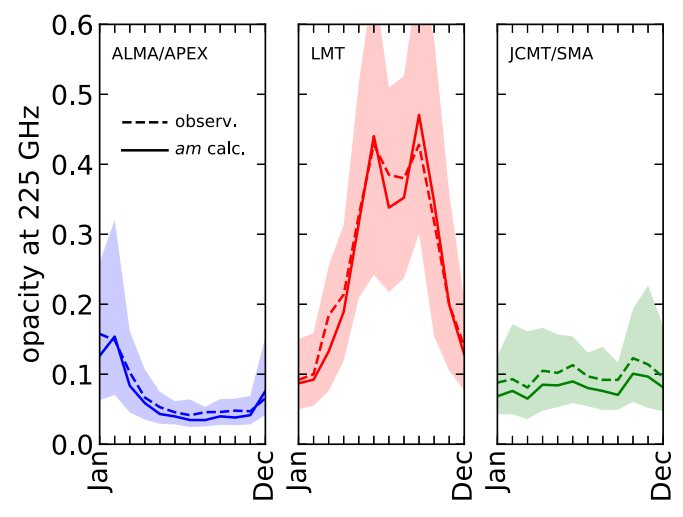


Figure 4. Monthly 225 GHz zenith opacity (τ_{225}) for three existing EHT sites. The calculated values (solid) from the reanalysis and 225 GHz radiometer observations (dashed) are comparable. The shaded region bounds the interquartile range, i.e., the middle 50% between the 25th (lower) and 75th (upper) percentiles for the reanalysis.

3. Results and Discussion

3.1. Weather and Observing Statistics

Figure 4 compares the 225 GHz opacity calculated with the am code using MERRA-2 data against the logged tipping radiometer measurements made at three different EHT sites. The tipping radiometer data sets are each multiyear: 1995–2004 for ALMA/APEX⁹, 2013–2017 for LMT (Ferrusca & Contreras 2014), and 2009–2014 for SMA (Radford & Peterson 2016). The tipper data were minimally flagged for τ_{225} extremes, and more than 95% of entries were kept for each site. The am calculation is for the same dates as the tipper entries except for APEX, which is done for our nominal 10 year period ending on the first day of 2019. The agreement between the medians of the calculations and field measurements supports our methods. The calculation reproduces the wide range of seasonal opacities between median $\tau_{225} = 0.04$ at APEX in July to $\tau_{225} = 0.47$ at LMT. Seasonal features, like the dip in July/August opacity at the LMT, are also reproduced. Figure 4 confirms that the calculation methods accurately reflect ensemble observing conditions at geographically varied sites.

Figure 5 plots the PWV statistics throughout the year at existing and candidate new sites. The northern sites (top row) generally exhibit minimum PWV values during December and January. Southern sites in the bottom row exhibit minimum PWV values during July and August. Historically, EHT observations are performed in March or April, when the northern sites still have reasonably dry atmospheres and ALMA has a median PWV column of 1–2 mm. All of the existing EHT sites have a median PWV column in March and April that is less than 5 mm. Most of the sites we analyze have comparable PWV statistics in those months.

The PWV averages we report, which are derived from the MERRA-2 data, agree with measurements available in the literature for both the 2021 array sites (plus ALMA) and for the candidate new sites. At the South Pole, which is presently the driest site in the array, radiosonde measurements collected over several decades show PWV ranges from about 0.25 mm in

http://legacy.nrao.edu/alma/site/

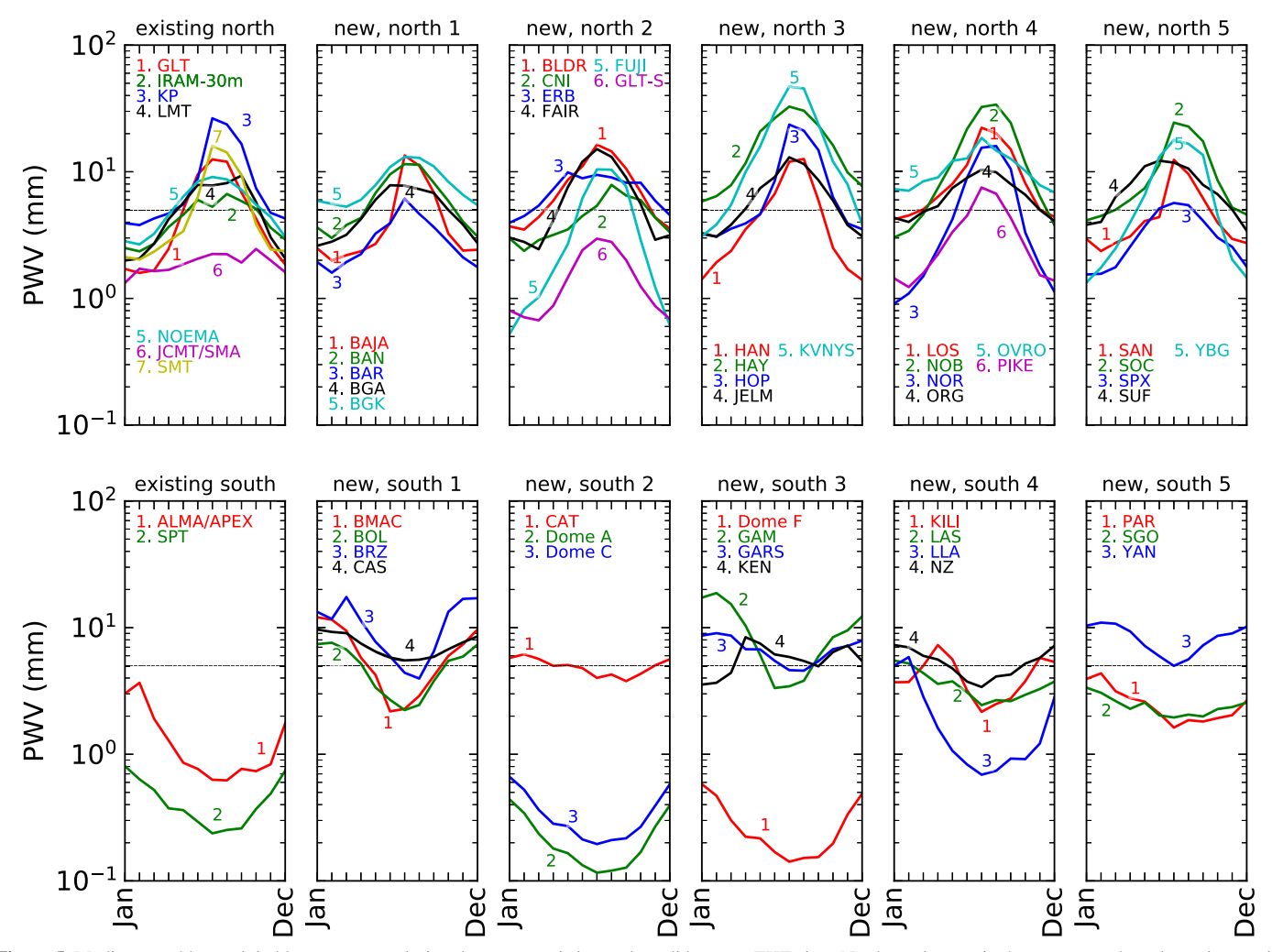


Figure 5. Median monthly precipitable water vapor during the year at existing and candidate new EHT sites. Northern sites are in the top row and southern sites are in the bottom row. In April, existing sites are below 5 mm, so a dotted line is added at that level.

July to just below 0.8 mm in January (Chamberlin 2001). The medians we derive for the SPT site are 0.24 mm in July and 0.8 mm in January. At Kitt Peak, multiyear infrared measurements done in the 1980s found median PWVs ranging from about 4 mm in winter to 27 mm in August during monsoon season (Wallace & Livingston 1984). We find 3.8–4.2 mm in winter and about 23 mm in August. Thus, for the driest and wettest sites in the EHT array, we find that the interpolated MERRA-2-based PWV agrees with what has been measured in the field.

PWV field measurements have also been made at many of the candidate new sites, and in most of those cases, we also find that the MERRA-2 PWV values are reliable. At Dome A and Dome C, the yearly median PWV values reported from satellite data from 2008 to 2010 are 0.21 and 0.28 mm, respectively (Tremblin et al. 2012). We find yearly medians of 0.19 and 0.29 mm for those sites, which are in good agreement as expected since the satellite data used would have been assimilated into MERRA-2. Ground-based radiometer measurements between 2009 and 2014 (Ricaud et al. 2015) observed mean seasonal PWV values of about 0.3 mm during June–August and about 0.7 mm in December–February. We find a similar range: 0.2 mm in June–August and 0.6 mm in December–February.

Precipitable water vapor measurements for Teide and Roque de los Muchachos Observatory in the Canary Islands were made using Global Positioning System path delays and radiosondes (Castro-Almazán et al. 2016). For the years 2012 and 2013, monthly median PWV values at CI ranged from about 2 mm in February to about 9 mm in August compared with our 10 year medians of 2.3 mm and 7.9 mm in February and August, respectively.

The European Southern Observatory performed a multi-instrument campaign involving optical, far-infrared, and radiosonde measurements at Paranal and La Silla (Querel et al. 2010). The study concluded that between 2005 and 2009, those sites had mean PWV columns of 2.3 ± 1.8 and 3.4 ± 2.4 mm, respectively. Those values are close to the mean of the monthly medians we obtain from interpolating MERRA-2 data: 2.6 mm at PAR and 3.6 mm at LAS. Both the Querel et al. (2010) result and our value agree with a two-year field measurement made using a 183 GHz radiometer (Kerber et al. 2015), which found 3.0 mm.

While the agreement with the literature is good for most of the sites we analyze, there are a few cases where the agreement is not as close. Far-infrared radiometer measurements made on intervals between 1984 and 1987 at Pico Veleta (Quesada 1989) returned median PWV values of

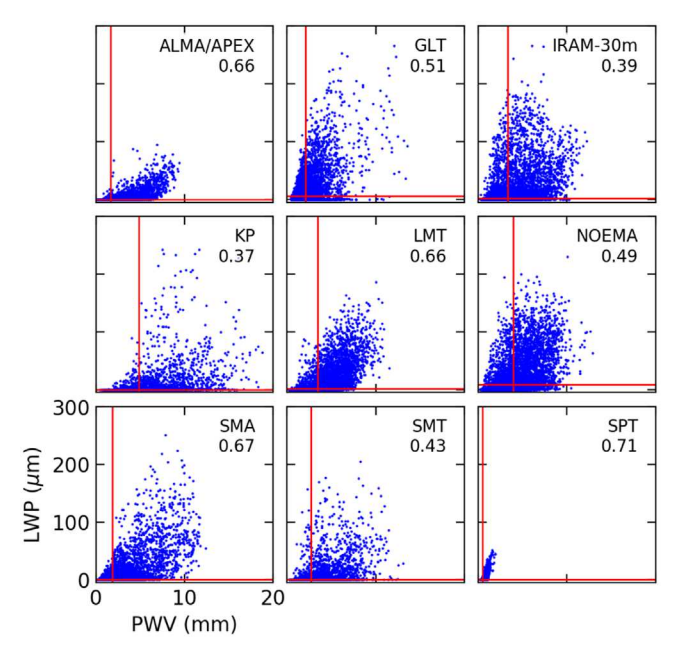


Figure 6. Precipitable water vapor and liquid water path for existing EHT sites during March and April. The Pearson correlation coefficient between PWV and LWP is listed below the site label. The vertical and horizontal lines show the median PWV and LWP, respectively.

1.2 mm in January up to 4.1 mm in September. We find slightly more water for IRAM-30 m: 2.5 mm in January and 6.7 mm in September. At JELM, field measurements beginning in the late 1970s found 1.4 mm of water vapor in winter up to 6.8 mm in August (Grasdalen et al. 1985). We find about 3.0 mm in winter and almost 12 mm in August. In these cases, discrepancies could be caused by local effects that the MERRA-2 profiles do not resolve. Future field measurements will be needed to determine if such anomalies exist at particular sites.

As we have already established, cloud liquid water also affects submillimeter opacity. In Figure 6, the LWP and PWV values at the existing EHT sites are plotted for each 3 hr bin in the MERRA-2 data set, and the median of each axis is marked with a red line. The correlation between the LWP and PWV variables ranges from weak to strong depending on the site, with the Pearson coefficient varying from about 0.3 to a little more than 0.7, and the maximum LWP values range from 50 μ m at the South Pole to approximately 200 μ m at several of the sites. Figure 7 shows the same information but for the candidate new sites. The LWP/PWV correlation coefficients have a similar range as the existing sites: approximately 0.3 to 0.75 with the exception of CAS. At the BAN, BGA, BGK, NOR, NZ, and SPX sites, there are a significant number of days when the vapor content is less than 5 mm, but the liquid content is approaching $100 \, \mu \text{m}$.

At some of the sites in Figures 6 and 7 there is only moderate correlation between the LWP and PWV statistics. The frequency of appreciable cloud cover is therefore important in its own right. In Table 3, we show the number of days per month with at least $50 \, \mu \mathrm{m}$ of LWP column on a bimonthly basis, which corresponds to a 0.13 and 0.18 opacity increase above the clear-sky conditions at 230 and 345 GHz, respectively.

In March, the existing EHT sites have an average of five or fewer days each month with heavy cloud cover. Twenty-five of the candidate new sites have a comparable frequency of clouded days and would therefore be similarly reliable for observing.

Unlike PWV statistics, which have a seasonality that depends strongly on hemisphere, the seasonality of cloud cover is more regional. For example, the sites in the southwestern United States have increased cloudiness in late summer because of the North American monsoon. Except for NOEMA, which does not exhibit much seasonal variation to begin with, none of the existing EHT sites has its greatest number of clouded days in March. This supports the idea that March and April are good months for EHT observations. Of the candidate new sites, some, like BGK and YAN, probably have a prohibitive number of clouded days throughout the year. Other sites show remarkable seasonal dependence. For example, GAM goes from eight clouded days in January to zero days throughout June and August. If the EHT eventually moves from once-per-year, campaign-style observations to remotely controlled observations that target the optimal conditions for each source, then it may be possible to capitalize on such variability.

While PWV and LWP are good indicators of observing conditions, radiative transfer at a particular site also depends on local vertical properties of moisture and temperature (Paine 2019) and must therefore be calculated. Table 4 presents the zenith 230 GHz opacity. Opacities are calculated using the local thermodynamic conditions above each site. Neither March nor April are extreme seasons for the 230 GHz zenith opacity. Of the candidate new sites, 21 of them have median zenith opacity of less than 0.2 during either of those months. The sites with median opacity below 0.10 (Dome A, Dome C, Dome F, FUJI, GLT-S, LLA, NOR, and PIKE) have interquartile ranges that vary from less than 0.01 at Antarctic sites to 0.2 elsewhere. A second tier of sites have opacities between 0.1 and 0.15 (BAJA, BAR, HAN, PAR, SGO, SPX, and YBG).

The opacities we report agree reasonably well with published field measurements. At the Greenland Summit site, a multiyear 225 GHz radiometer campaign beginning in 2010, found that the median opacity during the winter months was about 0.06 (Matsushita et al. 2017). We find a similar median opacity: 0.05 to 0.06. The median in July is also similar: 0.16–0.19 in the Matsushita et al. (2017) field measurement and 0.16 for our retrieval.

At the HAN site, 220 GHz tipping radiometer measurements beginning at the end of 1999 until the middle of 2001 have been published (Ananthasubramanian et al. 2002). The monthly median opacities reported are $0.07^{0.09}_{0.05}$ in January and $0.37^{0.46}_{0.26}$ in July. For 2009–2019, we calculate opacities of $0.07^{0.12}_{0.05}$ and $0.53^{0.69}_{0.37}$ in those months. The agreement in wintertime is excellent. In summer, additional field measurement data is needed to constrain the level of overlap between the experimental and model distributions.

The wintertime conditions at FUJI are very good and agree with previous 220 GHz radiometer measurements done 1994–1995 (Sekimoto et al. 1996). In December of 1994, an opacity of about 0.04 was measured, which matches exactly with the $0.04^{0.11}_{0.03}$ range from our calculation. The agreement in

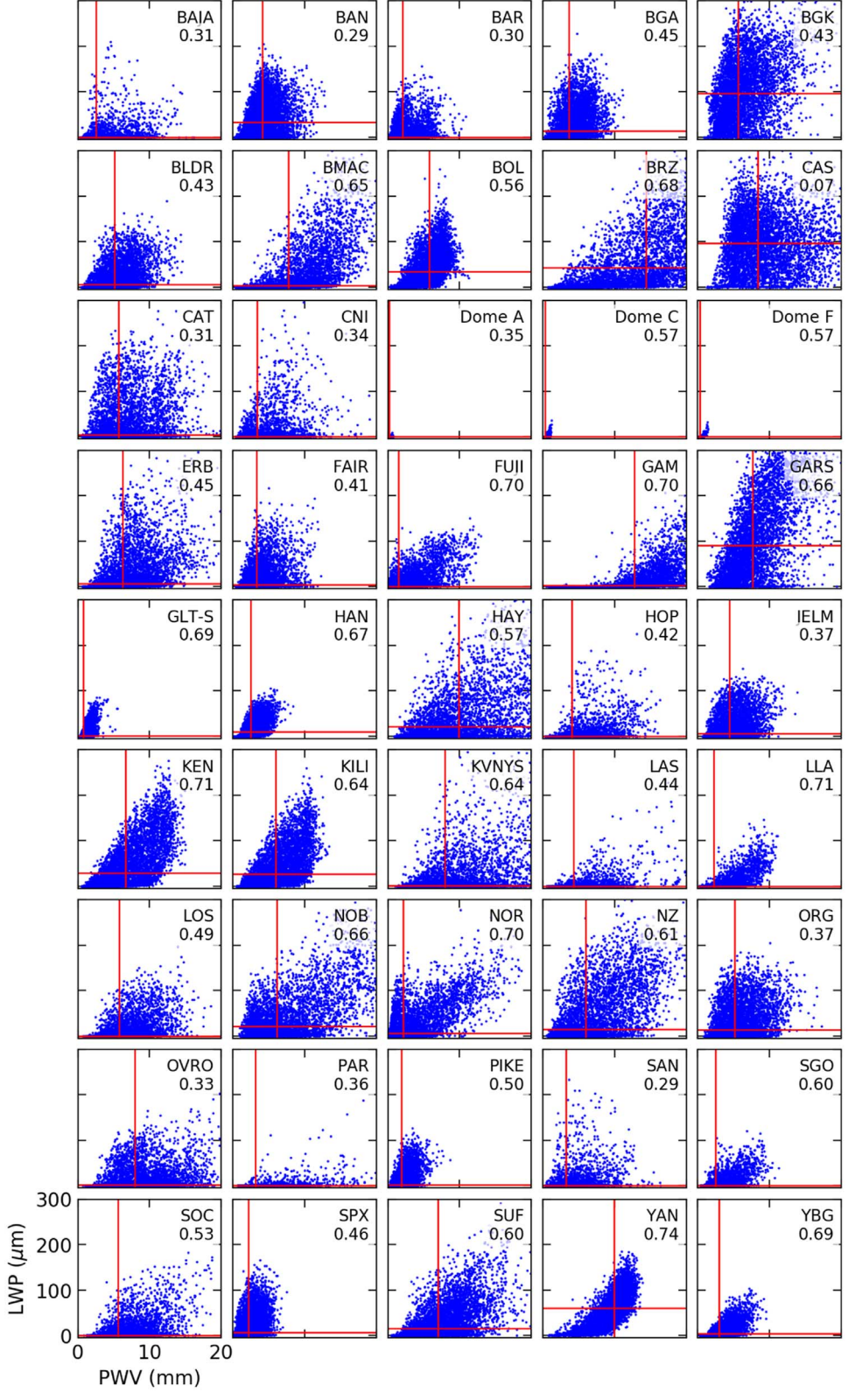


Figure 7. Same as Figure 6, but for candidate new sites.

March is also within the statistical variation: 0.11 observed compared with $0.06_{0.03}^{0.16}$ from our 10 year average. Mount Fuji has good submillimeter conditions in winter.

Finally, our opacity calculations agree with the 225 GHz tipping radiometer measurements for 2001 September to November, reported by Marvil et al. (2006) for the BAR site.

Site	Jan.	Mar.	May	Jul.	Sep.	Nov.
ALMA/APEX	120	010	000	000	000	
GLT	2_{1}^{4}	2_1^4	o_0^{11}	10_9^{13}	13_{12}^{16}	$0_0^0 \\ 7_6^9 \\ 4_3^6 \\ 4_3^6 \\ 2_4^2 \\ 1_1^2 \\ 2_4^4 \\ 5_4^7$
IRAM-30 m	2^{1}_{2}	46	9_8^{11} 3_2^5	0_0^0	24	76 16
JCMT/SMA	1_1^2	43 25	13	O_0	2_{2}^{4} 2_{1}^{3}	43 24
	2_{2}^{4}	3 ₂	1 ₁	0_0	∠ ₁	12
KP	01	4_{3}^{6} 3_{2}^{5} 1_{0}^{2} 2_{1}^{3}	1_{1}^{3} 0_{0}^{1} 7_{6}^{10}	0_0^1 9_8^{11} 10_9^{12}	4_3^6 15_{14}^{18}	1 ₁
LMT	0_0^1 4_3^5 2_1^3	2 ₁	1012	109	15 ₁₄	2 ₂
NOEMA	43	5_4^7	10_9^{12}	6_5^8	6_5^8 6_5^8	5 ₄
SMT		1_1^2	1_0^2	10_9^{12}	65	1_1^2
SPT	000	000	000	000	000	000
BAJA	1_1^3	0_0^1	0_0^1	34	2_{2}^{4}	0_0^1
BAN	65	11_{9}^{13}	1315	16_{15}^{19}	11_{9}^{13}	971
BAR	1_0^2	1_1^2	3_2^5	3_3^5	1_1^2	0_{0}^{1}
BGA	3_{2}^{4}	6_{5}^{8}	3_{2}^{5} 13_{12}^{15}	3_3^5 10_9^{12}	1_1^2 7_6^9	3_2^5
BGK	$ \begin{array}{c} 6_5^8 \\ 1_0^2 \\ 3_2^4 \\ 23_{22}^{25} \end{array} $	6_{5}^{8} 23_{21}^{25}	19_{18}^{22}	16_{15}^{18} 7_{6}^{9} 1_{0}^{2} 3_{2}^{4} 3_{3}^{5} 17_{16}^{19}	22_{21}^{24}	9_{7}^{11} 0_{0}^{1} 3_{2}^{5} 22_{21}^{24}
BLDR	214	3_3^5 8_6^{10} 13_{12}^{16} 17_{15}^{19}	7_{6}^{9}	7_{6}^{9}	5_4^6	$ \begin{array}{c} 22_{11} \\ 2_{1}^{3} \\ 4_{3}^{6} \\ 10_{9}^{12} \\ 16_{15}^{18} \end{array} $
BMAC	10_{9}^{13}	8_6^{10}	2_1^4	1_0^2	1_1^2	4_{3}^{6}
BOL	$17_{15}^{19} \\ 13_{12}^{16}$	13_{12}^{16}	5_4^7	3_{2}^{4}	8 ¹⁰ 5 ⁷	10_{9}^{12}
BRZ	13_{12}^{16}	17_{15}^{19}	7_{6}^{9}	$3^{\frac{1}{5}}_{3}$	57	16_{15}^{18}
CAS	26_{26}^{28}	23_{22}^{26}	19_{17}^{21}	17_{16}^{19}	18_{17}^{21}	24_{23}^{26}
CAT	57	68	912	810	810	810
CNI	5_4^7 1_1^2	6_5^8 2_1^3	9_8^{12} 0_0^0	8_{7}^{10} 0_{0}^{0} 0_{0}^{0} 0_{0}^{0} 0_{0}^{0} 0_{0}^{0} 19_{18}^{22}	8_{7}^{10} 0_{0}^{1}	8_7^{10} 2_2^4
Dome A	0_0^0	0_0^0	0_{0}^{0}	0_0°	0_0^0	00
Dome C	0_0^0	0_0^0	0_{0}^{0}	0_{0}^{2}	0_0^0	$\begin{array}{c} 0_0^0 \\ 0_0^0 \\ 0_0^0 \\ 0_0^0 \\ 5_4^7 \\ 4_3^6 \\ 2_2^4 \\ 1_1^2 \\ 21_{20}^{23} \\ 0_0^1 \\ 0_0^1 \\ 9_{17}^{17} \\ 1_1^2 \end{array}$
Dome F	0_{0}^{0}	0_0^0	0_0^0	O_0	0^{0}	0_{0}^{0}
ERB	0_0^0 5_4^7 3_3^5 1_0^2	0 ₀	0 ₀	O_0	0_0^0 0_0^1 10_9^{13}	57
FAIR	25 25	7_6^9	3_3^5 12_{11}^{14}	1022	1013	3 ₄
	3 ₃	3_2^4	12 ₁₁	1918	10 ₉	4 ₃
FUJI	$1_{\bar{0}}$	2 ⁴ ₂ 7 ⁹ ₆	$4_3^6 0_0^1$	10_9^{12}	7 ₆	2 ₂
GAM	$8_{7}^{10} \\ 22_{21}^{24}$	76	1020	0_0^0	0_0^1	1 <u>1</u>
GARS	2221	21_{20}^{24}	18_{16}^{20}	14_{13}^{17}	15_{14}^{17}	2120
GLT-S	0_0^0	0_0^0	1_0^2 3_2^5	l ₁ -10	l_1^{σ}	00
HAN	0_0^1	1_1^2	32	1_{1}^{2} 7_{6}^{10} 11_{10}^{13}	1_1^3 4_3^5 8_7^{10} 6_5^8	01
HAY	971	10_9^{13}	13_{11}^{15}	1113	87	97
HOP	2_{2}^{4}	1_0^2	0_{0}^{1}	12_{11}^{15}	6_{5}^{8}	1_1^2
JELM	2_1^3	3_2^5	7_{6}^{9}	6_5^8 11_{10}^{14}	4_3^6 8_7^{10} 1_0^2 7_6^9	2_1^4
KEN	4 ⁶ ₃ 5 ⁷ ₄	9_{7}^{11}	10_9^{12}	11_{10}^{14}	8_{7}^{10}	15^{18}_{14}
KILI	5_4^7	9_8^{12}	4_3^6	0_0^0	1_0^2	11_{10}^{13}
KVNYS	453	9_8^{12} 5_4^7	4_3^6 6_5^8 1_1^3	0_0^0 13_{11}^{15}	7_{6}^{9}	11_{10}^{13} 8_{7}^{10} 0_{0}^{0}
LAS	0_{0}^{0}	0_{0}^{1}	1_1^3	1_0^2	0_0^1	O_0^0
LLA	5_{4}^{7}	2_{1}^{3}	0_{0}^{0}	0_{0}^{0}	0_0^0 6_5^8 16_{14}^{18}	0_0^0 2_1^3
LOS	5_4^7 2_1^3 5_4^7	2_1^3	3_{2}^{4}	0_0^0 9_8^{11} 19_{18}^{21} 16_{14}^{18}	6^{8}_{5}	2^{3}_{1}
NOB	5^{7}_{4}	2_{1}^{3} 9_{8}^{11} 6_{5}^{8}	10_9^{12}	19^{21}_{18}	16^{18}_{14}	10_{9}^{12} 4_{3}^{6} 12_{11}^{14}
NOR	46	68	810	1618	1113	46
NZ	1214	911	1113	10^{12}	1114	1214
ORG	46	8 ¹⁰	79	12	24	57
OVRO	7 3	35	76 46	11 15	13	23
PAR	0^{0}	0^{0}	01	00	00	00
	1 ²	9_{8}^{11} 8_{6}^{10} 3_{2}^{5} 0_{0}^{0} 1_{1}^{3} 1_{0}^{2}	8_{7}^{10} 11_{10}^{13} 7_{6}^{9} 4_{3}^{6} 0_{0}^{1} 3_{3}^{5} 1_{0}^{2}	0 ₀	0 ₀	5_{4}^{7} 2_{1}^{3} 0_{0}^{0} 0_{0}^{2} 0_{0}^{1}
PIKE	23	11 12	33 12	07 25	13	0_0
SAN	Δ <u>Ϊ</u>	1 <u>0</u>	1 ₀	3 <u>5</u>	1 <u>1</u>	0.0
SGO	4_{3}^{6} 12_{10}^{14} 4_{3}^{6} 3_{2}^{4} 0_{0}^{0} 1_{0}^{2} 2_{1}^{3} 1_{0}^{2} 2_{1}^{3} 1_{2}^{4} 4_{3}^{5} 19_{17}^{21}	0_0^1	2_1^3	I_{l}^{\prime}	I_1^{\prime}	$0_0^1 \\ 1_1^3 \\ 3_2^4 \\ 3_2^5 \\ 12_{10}^{14}$
SOC	23	2_1^3	24/2	11_{10}^{13}	86	13
SPX	24	353 685 202319	12_{10}^{14}	1214	7^{9}_{5}	32
SUF	45	65	9811	1_1^2	0_0^2	35
YAN	19^{21}_{17}	20_{19}^{23}	9_8^{11} 9_8^{11} 4_3^6	$10_{8}^{12} \\ 1_{1}^{2} \\ 4_{3}^{5} \\ 0_{0}^{0} \\ 8_{7}^{10} \\ 3_{2}^{5} \\ 1_{1}^{3} \\ 11_{10}^{13} \\ 12_{11}^{14} \\ 1_{1}^{2} \\ 4_{3}^{6} \\ 16_{14}^{18}$	$\begin{array}{c} 11_{10}^{14} \\ 2_{2}^{4} \\ 2_{1}^{3} \\ 0_{0}^{0} \\ 3_{3}^{5} \\ 1_{1}^{3} \\ 1_{1}^{3} \\ 8_{6}^{10} \\ 7_{5}^{9} \\ 0_{0}^{2} \\ 9_{11}^{11} \\ 10_{9}^{12} \end{array}$	12_{10}^{14}
YBG	0_0^0	0_0^1	4_3^6	16^{18}_{14}	10_9^{12}	0_{0}^{0}

Note. Sub/superscripts are 25/75th percentiles, respectively.

The median measured opacity was 0.11 over that time frame, which is similar to the 0.11 to 0.17 10 year median values we calculate for the same months.

3.2. Applicability to 345 GHz and Higher Frequencies

The highest-frequency Fourier components (\vec{u}) sampled during the 230 GHz observation in 2017 of the M87* source were measured on the baseline between Hawaii and Spain (Event Horizon Telescope Collaboration et al. 2019a) and corresponded to 25 μ as instrumental angular resolution defined by the fringe spacing λ/D , where λ is the observing wavelength and D is the projected baseline length to the source. There is interest in operating at 345 GHz or potentially higher frequencies at the stations with suitable conditions, which could improve the nominal resolution by 50% or more. Most of the 2021 EHT sites are capable of 345 GHz operation during at least part of the year, and the transmittances $(Tr = -\ln \tau)$ of each existing site during March and April are plotted in Figure 8. Although the transmittance threshold for 345 GHz capability depends on the telescope sensitivity and other details like the atmospheric coherence, we can make a reasonable estimate of the transmittance that is required. Consider the case of a 0.1 Jy correlated flux density at 45° elevation with two-bit digital efficiency, and a 345 GHz zenith transmittance of 0.6 (opacity of 0.5) and sky-brightness temperature of 150 K. Under those conditions, two stations with 10 m diameter antennas having 64 μ m effective surfaceaccuracy apertures and 100 K receiver temperatures integrating for 100 s at 8 GHz fringe-finding bandwidth would achieve an S/N 3 detection. Stronger detections would be achieved on baselines to large apertures like ALMA or NOEMA.

The existing sites in Chile, Hawaii, and the South Pole have median March 345 GHz transmittance of 0.75 or greater. The South pole, in particular, has excellent 345 GHz transmittance even at the 25th percentile. The SPT site also has relatively good transmittance at 410 GHz (above 70%). Zenith transmission spectra for the new sites are plotted in Figure 9. Of these, Dome A , Dome C, and Dome F have high-frequency conditions that are similar to the SPT site. The FUJI, GLT-S, HAN, LLA, and PIKE sites are similar to the ALMA/APEX and JCMT/SMA sites: more opaque than Antarctica and more variable. BAJA, BAR, NOR, SGO, SPX, and YBG have comparable 345 GHz transmittance to the LMT site and would probably be viable during a useful fraction of time.

The high-frequency transmittances we calculate are in agreement with published values. At Dome C, the 345 GHz value for an atmosphere with the median PWV of 0.28 mm have been reported to be between 0.85 and 0.90 (Tremblin et al. 2012). At Dome A, that same study found 345 GHz transmittance in median conditions to be greater than 0.9. Both of those findings agree with the spectra we report specifically for March. At Yangbajing Observatory, for a median atmosphere containing 2.8 mm of water vapor, that same Tremblin et al. (2012) study concluded that YBG has 345 GHz transmittance of 55%–60%. In March, we derive a similar median PWV of 2.4 mm for the YBG site and correspondingly greater transmittance of about 0.67.

Table 4Zenith Opacity at 230 GHz

Site	Jan.	Feb.	Mar.	Apr.	May	Jun.	Jul.	Aug.	Sep.	Oct.	Nov.	Dec.
ALMA/APEX	$0.13_{0.06}^{0.26}$	$0.15_{0.07}^{0.31}$	$0.08_{0.04}^{0.16}$	$0.06_{0.03}^{0.11}$	$0.04_{0.03}^{0.07}$	$0.04_{0.03}^{0.06}$	$0.03_{0.02}^{0.06}$	$0.03_{0.03}^{0.05}$	$0.04_{0.03}^{0.06}$	$0.04_{0.03}^{0.06}$	$0.04_{0.03}^{0.07}$	$0.07_{0.04}^{0.15}$
GLT	$0.16_{0.13}^{0.26}$	$0.15_{0.12}^{0.25}$	$0.15_{0.13}^{0.24}$	$0.21_{0.16}^{0.31}$	$0.37_{0.29}^{0.58}$	$0.65_{0.53}^{0.94}$	$0.84_{0.69}^{1.17}$	$0.82^{1.27}_{0.62}$	$0.53_{0.39}^{0.82}$	$0.37_{0.24}^{0.60}$	$0.24_{0.17}^{0.40}$	$0.17_{0.13}^{0.30}$
IRAM-30 m	$0.14_{0.08}^{0.24}$	$0.13^{0.24}_{0.07}$	$0.15_{0.08}^{0.29}$	$0.20_{0.12}^{0.34}$	$0.24_{0.14}^{0.37}$	$0.30_{0.20}^{0.43}$	$0.26_{0.16}^{0.40}$	$0.33_{0.21}^{0.49}$	$0.29_{0.19}^{0.45}$	$0.26_{0.15}^{0.42}$	$0.19_{0.11}^{0.36}$	$0.15_{0.08}^{0.27}$
JCMT/SMA	$0.06_{0.04}^{0.12}$	$0.08^{0.17}_{0.04}$	$0.08_{0.04}^{0.20}$	$0.08^{0.16}_{0.05}$	$0.08_{0.05}^{0.16}$	$0.09_{0.06}^{0.15}$	$0.11_{0.06}^{0.17}$	$0.09_{0.06}^{0.21}$	$0.08_{0.05}^{0.17}$	$0.11^{0.22}_{0.06}$	$0.09_{0.05}^{0.21}$	$0.07_{0.04}^{0.17}$
KP	$0.21_{0.13}^{0.40}$	$0.21_{0.13}^{0.36}$	$0.24_{0.15}^{0.37}$	$0.25_{0.16}^{0.37}$	$0.29_{0.20}^{0.43}$	$0.45_{0.26}^{0.78}$	$1.47_{1.11}^{1.77}$	$1.31_{0.97}^{1.66}$	$0.92^{1.31}_{0.54}$	$0.40_{0.25}^{0.65}$	$0.26_{0.16}^{0.42}$	$0.24_{0.14}^{0.40}$
LMT	$0.09_{0.05}^{0.15}$	$0.09_{0.05}^{0.16}$	$0.13_{0.06}^{0.21}$	$0.19_{0.12}^{0.33}$	$0.25_{0.15}^{0.45}$	$0.40_{0.20}^{0.63}$	$0.37_{0.22}^{0.56}$	$0.39_{0.26}^{0.58}$	$0.49_{0.31}^{0.69}$	$0.26_{0.11}^{0.46}$	$0.14_{0.07}^{0.27}$	$0.09_{0.05}^{0.16}$
NOEMA	$0.16_{0.09}^{0.29}$	$0.16_{0.09}^{0.30}$	$0.19_{0.12}^{0.33}$	$0.27_{0.17}^{0.45}$	$0.37_{0.22}^{0.62}$	$0.46_{0.31}^{0.71}$	$0.48_{0.31}^{0.69}$	$0.45_{0.29}^{0.67}$	$0.39_{0.24}^{0.60}$	$0.29_{0.16}^{0.51}$	$0.25_{0.14}^{0.45}$	$0.17_{0.09}^{0.31}$
SMT	$0.12_{0.07}^{0.20}$	$0.11_{0.06}^{0.19}$	$0.13_{0.07}^{0.20}$	$0.15_{0.09}^{0.22}$	$0.17_{0.12}^{0.26}$	$0.30_{0.16}^{0.51}$	$0.82^{1.05}_{0.60}$	$0.73_{0.51}^{0.99}$	$0.48_{0.29}^{0.73}$	$0.19_{0.12}^{0.34}$	$0.13_{0.07}^{0.22}$	$0.13_{0.07}^{0.21}$
SPT	$0.06^{0.07}_{0.05}$	$0.05^{0.06}_{0.05}$	$0.05^{0.05}_{0.04}$	$0.04_{0.04}^{0.05}$	$0.04_{0.04}^{0.05}$	$0.04_{0.03}^{0.04}$	$0.04_{0.03}^{0.04}$	$0.04_{0.03}^{0.04}$	$0.04_{0.03}^{0.04}$	$0.04_{0.04}^{0.05}$	$0.04_{0.04}^{0.05}$	$0.06_{0.05}^{0.07}$
BAJA	$0.13^{0.25}_{0.07}$	$0.11_{0.06}^{0.20}$	$0.12^{0.21}_{0.07}$	$0.13^{0.21}_{0.07}$	$0.14_{0.09}^{0.21}$	$0.19_{0.12}^{0.39}$	$0.67_{0.40}^{0.94}$	$0.56_{0.31}^{0.82}$	$0.34_{0.16}^{0.62}$	$0.16^{0.27}_{0.09}$	$0.13^{0.21}_{0.07}$	$0.13_{0.07}^{0.22}$
BAN	$0.24_{0.14}^{0.42}$	$0.20_{0.12}^{0.37}$	$0.27_{0.16}^{0.45}$	$0.30_{0.20}^{0.49}$	$0.43_{0.29}^{0.65}$	$0.62_{0.45}^{0.89}$	$0.69_{0.51}^{0.99}$	$0.65_{0.49}^{0.94}$	$0.48_{0.33}^{0.73}$	$0.36_{0.22}^{0.58}$	$0.27_{0.16}^{0.46}$	$0.21_{0.13}^{0.36}$
BAR	$0.11_{0.05}^{0.17}$	$0.08_{0.05}^{0.14}$	$0.11_{0.06}^{0.16}$	$0.12^{0.19}_{0.07}$	$0.16^{0.25}_{0.11}$	$0.19_{0.12}^{0.29}$	$0.29_{0.16}^{0.48}$	$0.21_{0.13}^{0.37}$	$0.17_{0.11}^{0.27}$	$0.14_{0.08}^{0.21}$	$0.11_{0.06}^{0.16}$	$0.09_{0.05}^{0.16}$
BGA	$0.15_{0.09}^{0.26}$	$0.16_{0.11}^{0.27}$	$0.19_{0.11}^{0.33}$	$0.25_{0.14}^{0.43}$	$0.37_{0.24}^{0.60}$	$0.46_{0.29}^{0.73}$	$0.42^{0.67}_{0.27}$	$0.39_{0.26}^{0.58}$	$0.36_{0.21}^{0.58}$	$0.26_{0.13}^{0.45}$	$0.21_{0.12}^{0.33}$	$0.15_{0.08}^{0.26}$
BGK	$0.58_{0.34}^{0.94}$	$0.54_{0.31}^{0.89}$	$0.51_{0.29}^{0.87}$	$0.54_{0.30}^{0.94}$	$0.62^{1.08}_{0.37}$	$0.76^{1.20}_{0.51}$	$0.89_{0.65}^{1.39}$	$0.92^{1.47}_{0.63}$	$0.89_{0.54}^{1.43}$	$0.73_{0.43}^{1.17}$	$0.60^{1.02}_{0.34}$	$0.53_{0.29}^{0.92}$
BLDR	$0.21_{0.13}^{0.30}$	$0.20_{0.14}^{0.33}$	$0.24_{0.16}^{0.36}$	$0.31_{0.24}^{0.48}$	$0.46_{0.33}^{0.63}$	$0.54_{0.39}^{0.76}$	$0.84_{0.62}^{1.11}$	$0.73_{0.54}^{0.99}$	$0.53_{0.37}^{0.76}$	$0.36_{0.25}^{0.51}$	$0.24_{0.15}^{0.34}$	$0.20_{0.13}^{0.30}$
BMAC	$0.63_{0.40}^{0.99}$	$0.62^{1.02}_{0.36}$	$0.49_{0.29}^{0.76}$	$0.30_{0.16}^{0.53}$	$0.22_{0.13}^{0.39}$	$0.12^{0.24}_{0.07}$	$0.13_{0.07}^{0.22}$	$0.16_{0.08}^{0.29}$	$0.21_{0.12}^{0.39}$	$0.30_{0.17}^{0.51}$	$0.37_{0.22}^{0.60}$	$0.49_{0.30}^{0.80}$
BOL	$0.39_{0.27}^{0.51}$	$0.42^{0.54}_{0.29}$	$0.34_{0.22}^{0.49}$	$0.24_{0.14}^{0.40}$	$0.15_{0.08}^{0.29}$	$0.12^{0.24}_{0.05}$	$0.09_{0.05}^{0.20}$	$0.11_{0.05}^{0.22}$	$0.17_{0.08}^{0.34}$	$0.27_{0.14}^{0.43}$	$0.27_{0.16}^{0.43}$	$0.37_{0.25}^{0.51}$
BRZ	$0.71_{0.34}^{1.35}$	$0.63_{0.36}^{1.14}$	$0.97_{0.54}^{1.47}$	$0.63_{0.31}^{1.14}$	$0.43_{0.21}^{0.76}$	$0.33_{0.15}^{0.58}$	$0.24_{0.11}^{0.46}$	$0.22_{0.09}^{0.45}$	$0.36_{0.13}^{0.69}$	$0.71_{0.36}^{1.17}$	$0.94_{0.49}^{1.47}$	$0.94_{0.54}^{1.51}$
CAS	$0.80_{0.53}^{1.27}$	$0.76^{1.24}_{0.48}$	$0.71_{0.46}^{1.17}$	$0.60^{1.02}_{0.37}$	$0.49_{0.33}^{0.82}$	$0.48_{0.31}^{0.78}$	$0.45_{0.27}^{0.73}$	$0.46_{0.29}^{0.76}$	$0.48_{0.30}^{0.78}$	$0.54_{0.34}^{0.89}$	$0.63_{0.42}^{1.05}$	$0.73^{1.14}_{0.48}$
CAT	$0.31_{0.20}^{0.53}$	$0.34_{0.20}^{0.58}$	$0.31_{0.19}^{0.54}$	$0.29_{0.15}^{0.54}$	$0.31_{0.14}^{0.62}$	$0.30_{0.15}^{0.54}$	$0.26_{0.13}^{0.48}$	$0.29_{0.13}^{0.54}$	$0.24_{0.13}^{0.48}$	$0.27_{0.15}^{0.49}$	$0.29_{0.17}^{0.51}$	$0.31_{0.20}^{0.58}$
CNI	$0.16_{0.09}^{0.27}$	$0.13_{0.08}^{0.25}$	$0.16_{0.08}^{0.27}$	$0.16_{0.11}^{0.29}$	$0.19_{0.12}^{0.30}$	$0.22_{0.15}^{0.37}$	$0.26_{0.15}^{0.46}$	$0.39_{0.20}^{0.60}$	$0.33_{0.20}^{0.54}$	$0.30_{0.17}^{0.53}$	$0.22_{0.12}^{0.42}$	$0.17_{0.09}^{0.34}$
Dome A	$0.03^{0.04}_{0.03}$	$0.03_{0.03}^{0.03}$	$0.03_{0.02}^{0.03}$	$0.02^{0.03}_{0.02}$	$0.02^{0.03}_{0.02}$	$0.02^{0.03}_{0.02}$	$0.02^{0.03}_{0.02}$	$0.02_{0.02}^{0.02}$	$0.02_{0.02}^{0.02}$	$0.02_{0.02}^{0.03}$	$0.03_{0.03}^{0.03}$	$0.03_{0.03}^{0.04}$
Dome C	$0.05_{0.04}^{0.06}$	$0.04_{0.04}^{0.05}$	$0.04_{0.03}^{0.04}$	$0.03_{0.03}^{0.04}$	$0.03^{0.04}_{0.03}$	$0.03_{0.03}^{0.03}$	$0.03_{0.03}^{0.03}$	$0.03_{0.03}^{0.04}$	$0.03_{0.03}^{0.03}$	$0.03_{0.03}^{0.04}$	$0.04_{0.03}^{0.04}$	$0.05_{0.04}^{0.05}$
Dome F	$0.04_{0.04}^{0.05}$	$0.04_{0.03}^{0.04}$	$0.03_{0.03}^{0.03}$	$0.03_{0.03}^{0.03}$	$0.03_{0.03}^{0.03}$	$0.03_{0.02}^{0.03}$	$0.03^{0.03}_{0.02}$	$0.03_{0.02}^{0.03}$	$0.03^{0.03}_{0.02}$	$0.03_{0.03}^{0.03}$	$0.03^{0.04}_{0.03}$	$0.04_{0.03}^{0.04}$
ERB	$0.24_{0.15}^{0.40}$	$0.27_{0.15}^{0.43}$	$0.31_{0.20}^{0.51}$	$0.42^{0.62}_{0.27}$	$0.54_{0.39}^{0.73}$	$0.48_{0.33}^{0.65}$	$0.49_{0.33}^{0.71}$	$0.46_{0.31}^{0.63}$	$0.43_{0.30}^{0.58}$	$0.45_{0.29}^{0.67}$	$0.33_{0.19}^{0.54}$	$0.26_{0.15}^{0.46}$
FAIR	$0.21_{0.11}^{0.34}$	$0.20_{0.13}^{0.31}$	$0.17_{0.11}^{0.29}$	$0.27_{0.19}^{0.42}$	$0.49_{0.36}^{0.78}$	$0.80^{1.14}_{0.60}$	$1.02_{0.78}^{1.43}$	$0.87_{0.65}^{1.27}$	$0.56_{0.39}^{0.84}$	$0.36_{0.24}^{0.53}$	$0.20^{0.36}_{0.13}$	$0.22_{0.14}^{0.36}$
FUJI	$0.04_{0.03}^{0.08}$	$0.05_{0.03}^{0.13}$	$0.06_{0.03}^{0.16}$	$0.08^{0.22}_{0.04}$	$0.13^{0.34}_{0.05}$	$0.29_{0.12}^{0.63}$	$0.49_{0.29}^{0.80}$	$0.49_{0.29}^{0.76}$	$0.34_{0.13}^{0.63}$	$0.13_{0.05}^{0.39}$	$0.07_{0.03}^{0.19}$	$0.04_{0.03}^{0.11}$
GAM	$0.94_{0.60}^{1.35}$	$1.02_{0.60}^{1.51}$	$0.84_{0.53}^{1.24}$	$0.56_{0.34}^{0.82}$	$0.33_{0.21}^{0.48}$	$0.19_{0.11}^{0.29}$	$0.19_{0.11}^{0.30}$	$0.20_{0.12}^{0.33}$	$0.30_{0.14}^{0.51}$	$0.42_{0.21}^{0.63}$	$0.48_{0.25}^{0.73}$	$0.62_{0.39}^{0.94}$
GARS	$0.71_{0.51}^{1.14}$	$0.76^{1.20}_{0.51}$	$0.78^{1.24}_{0.48}$	$0.60^{1.05}_{0.34}$	$0.58_{0.33}^{1.05}$	$0.53_{0.27}^{0.94}$	$0.40^{0.82}_{0.21}$	$0.40^{0.82}_{0.21}$	$0.48_{0.25}^{0.94}$	$0.58_{0.34}^{1.05}$	$0.62_{0.42}^{1.05}$	$0.67_{0.48}^{1.05}$
GLT-S	$0.06^{0.09}_{0.05}$	$0.06^{0.08}_{0.05}$	$0.05^{0.08}_{0.04}$	$0.06_{0.05}^{0.11}$	$0.09_{0.07}^{0.15}$	$0.13_{0.09}^{0.20}$	$0.16^{0.22}_{0.12}$	$0.15_{0.12}^{0.24}$	$0.13^{0.20}_{0.08}$	$0.08^{0.14}_{0.06}$	$0.06_{0.05}^{0.11}$	$0.05^{0.08}_{0.04}$
HAN	$0.07_{0.05}^{0.12}$	$0.11_{0.07}^{0.15}$	$0.12^{0.19}_{0.08}$	$0.17_{0.12}^{0.25}$	$0.22_{0.15}^{0.31}$	$0.30_{0.21}^{0.43}$	$0.53_{0.37}^{0.69}$	$0.56_{0.37}^{0.71}$	$0.26_{0.15}^{0.45}$	$0.12_{0.08}^{0.16}$	$0.08_{0.06}^{0.13}$	$0.07^{0.11}_{0.05}$
HAY	$0.42_{0.22}^{0.73}$	$0.45_{0.26}^{0.82}$	$0.54_{0.30}^{0.99}$	$0.78_{0.48}^{1.35}$	1.35 ^{2.21} 0.240.36	$1.77_{1.20}^{2.66}$	$2.21^{3.00}_{1.56}$	$2.04_{1.43}^{2.81}$	1.512.41	$1.05^{1.83}_{0.65}$	$0.65_{0.39}^{1.14}$	$0.53_{0.31}^{0.97}$
HOP	$0.17_{0.11}^{0.31}$	$0.17^{0.30}_{0.11}$	$0.19_{0.12}^{0.30}$	$0.21_{0.14}^{0.31}$	$0.24_{0.16}^{0.36}$	$0.42_{0.25}^{0.73}$	1.27 ^{1.61} _{0.99}	$1.14_{0.87}^{1.51}$	$0.80_{0.49}^{1.17}$	$0.33_{0.20}^{0.56}$	$0.21_{0.13}^{0.34}$	$0.19_{0.11}^{0.33}$
JELM	$0.19_{0.11}^{0.27}$	$0.17_{0.12}^{0.30}$	$0.21_{0.14}^{0.31}$	$0.27_{0.20}^{0.42}$	$0.39_{0.29}^{0.54}$	$0.45^{0.60}_{0.31}$	$0.65_{0.46}^{0.89}$	$0.58_{0.42}^{0.80}$	$0.43_{0.29}^{0.62}$	$0.30_{0.21}^{0.45}$	$0.20^{0.30}_{0.13}$	$0.17_{0.11}^{0.27}$
KEN	$0.16^{0.31}_{0.09}$	$0.17_{0.09}^{0.34}$	$0.22_{0.11}^{0.48}$	$0.46_{0.26}^{0.71}$	$0.39_{0.24}^{0.60}$	$0.33_{0.20}^{0.54}$	$0.34_{0.19}^{0.53}$	$0.31_{0.16}^{0.53}$	$0.26_{0.16}^{0.45}$	$0.34_{0.21}^{0.54}$	$0.43_{0.27}^{0.63}$	$0.30_{0.17}^{0.51}$
KILI	$0.19_{0.09}^{0.37}$	$0.17^{0.39}_{0.09}$	$0.26_{0.13}^{0.49}$	$0.37_{0.21}^{0.58}$	$0.26_{0.15}^{0.42}$	$0.15^{0.24}_{0.08}$	$0.09_{0.06}^{0.17}$	$0.12_{0.06}^{0.21}$	$0.13^{0.21}_{0.08}$	$0.17^{0.33}_{0.09}$	$0.31_{0.17}^{0.51}$	$0.31_{0.17}^{0.51}$
KVNYS	$0.24_{0.16}^{0.40}$	$0.29_{0.17}^{0.49}$	$0.39_{0.24}^{0.63}$	$0.65_{0.42}^{1.05}$	$1.02_{0.67}^{1.56}$	$1.97^{2.53}_{1.43}$	$3.22_{2.41}^{3.91}$	$3.00^{3.91}_{2.21}$	$1.56_{1.05}^{2.30}$	$0.80^{1.24}_{0.53}$	$0.56_{0.31}^{0.99}$	$0.29_{0.17}^{0.53}$
LAS	$0.29_{0.17}^{0.46}$	$0.27_{0.17}^{0.42}$	$0.22_{0.15}^{0.34}$	$0.19_{0.13}^{0.29}$	$0.20^{0.30}_{0.13}$	$0.16_{0.11}^{0.26}$	$0.14_{0.08}^{0.22}$	$0.14_{0.09}^{0.22}$	$0.14_{0.09}^{0.22}$	$0.15^{0.24}_{0.11}$	$0.17_{0.12}^{0.25}$	$0.20^{0.29}_{0.13}$
LLA	$0.22_{0.11}^{0.40}$	$0.26_{0.12}^{0.46}$	$0.13_{0.06}^{0.22}$	$0.07^{0.13}_{0.04}$	$0.05^{0.08}_{0.03}$	$0.04_{0.03}^{0.06}$	$0.04_{0.03}^{0.06}$	$0.04_{0.03}^{0.06}$	$0.05^{0.07}_{0.03}$	$0.04_{0.03}^{0.07}$	$0.06^{0.09}_{0.04}$	$0.12_{0.06}^{0.25}$
LOS	$0.24_{0.16}^{0.36}$	$0.26_{0.17}^{0.36}$	$0.27_{0.19}^{0.39}$	$0.34_{0.24}^{0.46}$	$0.42^{0.58}_{0.30}$	$0.56_{0.34}^{0.87}$	$1.17_{0.92}^{1.47}$	$1.08_{0.80}^{1.35}$	$0.80^{1.11}_{0.53}$	$0.43_{0.29}^{0.63}$	$0.27_{0.17}^{0.40}$	$0.25_{0.16}^{0.37}$
NOB	$0.24_{0.16}^{0.40}$	$0.25_{0.16}^{0.48}$	$0.31_{0.19}^{0.63}$	$0.46^{0.89}_{0.27}$	$0.71_{0.42}^{1.24}$	$1.35_{0.89}^{2.12}$	$2.04_{1.51}^{2.66}$	$2.12_{1.61}^{2.81}$	1.512.30	$0.73_{0.43}^{1.43}$	$0.43_{0.26}^{0.80}$	$0.29_{0.19}^{0.49}$
NOR NZ	$0.08^{0.17}_{0.04}$	$0.08_{0.04}^{0.21} \ 0.40_{0.24}^{0.76}$	$0.09_{0.05}^{0.26}$	$0.14_{0.06}^{0.37}$	$0.21_{0.09}^{0.54}$	$0.48^{0.99}_{0.22}$	$0.84_{0.51}^{1.31}$	$0.87_{0.53}^{1.35}$	$0.53^{1.05}_{0.17}$	$0.16^{0.53}_{0.06}$	$0.12_{0.05}^{0.29}$	$0.09_{0.05}^{0.21}$
ORG	$0.43_{0.24}^{0.87} \\ 0.24_{0.13}^{0.42}$	$0.40_{0.24}^{0.40}$ $0.24_{0.15}^{0.40}$	$0.34_{0.19}^{0.71}$	$0.34_{0.17}^{0.69}$	$0.30_{0.17}^{0.58} \ 0.42_{0.27}^{0.62}$	$0.24_{0.13}^{0.48}$	$0.24_{0.12}^{0.45} \\ 0.53_{0.37}^{0.73}$	$0.29_{0.14}^{0.53}$	$0.30_{0.15}^{0.56} \\ 0.42_{0.29}^{0.58}$	$0.34_{0.17}^{0.62} \\ 0.36_{0.22}^{0.51}$	$0.37_{0.21}^{0.69} \\ 0.27_{0.15}^{0.45}$	$0.43_{0.24}^{0.82}$ $0.24_{0.13}^{0.43}$
OVRO	$0.24_{0.13}$ $0.42_{0.24}^{0.69}$	$0.24_{0.15}$ $0.42_{0.31}^{0.56}$	$0.27_{0.17}^{0.49} \ 0.49_{0.33}^{0.65}$	$0.30_{0.20}^{0.49}$ $0.51_{0.39}^{0.69}$	$0.42_{0.27} \\ 0.67_{0.48}^{0.89}$	$0.46_{0.33}^{0.65} \ 0.67_{0.48}^{0.94}$	$0.33_{0.37} \\ 0.97_{0.60}^{1.43}$	$0.51_{0.37}^{0.69} \\ 0.76_{0.51}^{1.17}$	$0.42_{0.29} \\ 0.67_{0.48}^{0.97}$	$0.56_{0.40}^{0.80}$	$0.27_{0.15}$ $0.45_{0.31}^{0.65}$	
	$0.42_{0.24} \\ 0.20_{0.12}^{0.33}$	$0.42_{0.31} \\ 0.21_{0.14}^{0.39}$	$0.49_{0.33}$ $0.16_{0.12}^{0.26}$	$0.51_{0.39}$ $0.14_{0.09}^{0.22}$	$0.67_{0.48}^{0.48}$ $0.13_{0.09}^{0.21}$	$0.67_{0.48}$ $0.11_{0.07}^{0.17}$					$0.43_{0.31}$ $0.11_{0.08}^{0.15}$	$0.40^{0.62}_{0.26}$
PAR					0.13 _{0.09}		$0.09_{0.06}^{0.14}$	$0.09_{0.07}^{0.15}$	$0.09_{0.06}^{0.15}$	$0.11_{0.07}^{0.15}$	0.11 _{0.08}	$0.14_{0.09}^{0.21}$
PIKE	$0.07_{0.05}^{0.12}$ $0.15_{0.08}^{0.27}$	$0.07_{0.04}^{0.11}$ $0.13_{0.07}^{0.22}$	$0.08_{0.05}^{0.13}$ $0.15_{0.08}^{0.25}$	$0.12_{0.07}^{0.19} \ 0.16_{0.11}^{0.26}$	$0.16_{0.11}^{0.26} \ 0.21_{0.13}^{0.33}$	$0.20_{0.13}^{0.31} \\ 0.21_{0.13}^{0.36}$	$0.36_{0.22}^{0.54} \ 0.63_{0.27}^{0.92}$	$0.31_{0.21}^{0.48} \ 0.48_{0.26}^{0.78}$	$0.20_{0.12}^{0.33} \\ 0.31_{0.17}^{0.54}$	$0.12_{0.07}^{0.19} \\ 0.20_{0.12}^{0.33}$	$0.08_{0.05}^{0.12} \ 0.15_{0.09}^{0.25}$	$0.07_{0.05}^{0.11}$ $0.15_{0.08}^{0.26}$
SAN SGO	$0.15_{0.08}^{0.26}$ $0.16_{0.11}^{0.26}$	$0.13_{0.07}^{0.25}$ $0.15_{0.09}^{0.25}$	$0.13_{0.08}^{0.20}$ $0.13_{0.08}^{0.20}$	$0.16_{0.11}^{0.11}$ $0.12_{0.07}^{0.19}$	$0.21_{0.13}^{0.21}$ $0.13_{0.07}^{0.21}$	$0.21_{0.13}^{0.13}$ $0.11_{0.06}^{0.19}$	$0.63_{0.27}^{0.17}$ $0.11_{0.06}^{0.17}$	$0.48_{0.26}^{0.19}$ $0.11_{0.06}^{0.19}$	$0.31_{0.17}^{0.17}$ $0.11_{0.06}^{0.17}$	$0.20_{0.12}^{0.12}$ $0.12_{0.07}^{0.19}$	$0.13_{0.09}^{0.19}$ $0.12_{0.08}^{0.19}$	$0.13_{0.08}^{0.20}$ $0.13_{0.08}^{0.20}$
	$0.16_{0.11}^{0.11}$ $0.24_{0.15}^{0.37}$	$0.15_{0.09}$ $0.25_{0.16}^{0.37}$	$0.13_{0.08}^{0.08}$ $0.27_{0.19}^{0.39}$	$0.12_{0.07}^{0.07}$ $0.31_{0.22}^{0.45}$	$0.13_{0.07}^{0.07}$ $0.39_{0.26}^{0.54}$	$0.11_{0.06}^{0.06}$ $0.56_{0.34}^{0.89}$	$1.31_{1.05}^{1.66}$	$0.11_{0.06}^{0.06}$ $1.24_{0.94}^{1.56}$	$0.11_{0.06}^{0.06}$ $0.94_{0.62}^{1.27}$	$0.12_{0.07}^{0.07}$ $0.45_{0.30}^{0.69}$	$0.12_{0.08}^{0.08}$ $0.29_{0.17}^{0.43}$	$0.13_{0.08}^{0.08}$ $0.26_{0.16}^{0.42}$
SOC		$0.25_{0.16}^{0.16}$ $0.09_{0.05}^{0.17}$										
SPX SUF	$0.09_{0.05}^{0.17} \\ 0.22_{0.13}^{0.37}$	$0.09_{0.05}^{0.05}$ $0.25_{0.13}^{0.43}$	$0.11_{0.06}^{0.19}$	$0.15_{0.08}^{0.27}$ $0.46_{0.29}^{0.71}$	$0.24_{0.13}^{0.40}$	$0.30_{0.16}^{0.49} \ 0.65_{0.49}^{0.87}$	$0.30_{0.16}^{0.53}$	$0.29_{0.16}^{0.51}$ $0.54_{0.40}^{0.73}$	$0.21_{0.12}^{0.39}$	$0.15^{0.27}_{0.08}$ $0.36^{0.54}$	$0.14_{0.07}^{0.25}$	$0.09_{0.06}^{0.19}$
	0.22 _{0.13}	$0.25_{0.13}^{0.13}$ $0.60_{0.48}^{0.71}$	$0.37_{0.22}^{0.60} \\ 0.60_{0.46}^{0.71}$	$0.46_{0.29}^{0.63}$ $0.49_{0.34}^{0.63}$	$0.62_{0.43}^{0.89} \ 0.37_{0.24}^{0.53}$	$0.65_{0.49}^{0.49}$ $0.29_{0.19}^{0.43}$	$0.62_{0.48}^{0.78} \ 0.24_{0.14}^{0.39}$		$0.42^{0.54}_{0.30}$	$0.36_{0.22}^{0.54} \ 0.43_{0.29}^{0.56}$	$0.29_{0.16}^{0.45} \ 0.45_{0.29}^{0.60}$	$0.20^{0.36}_{0.11}$
YAN VRC	$0.56_{0.42}^{0.67} \\ 0.07_{0.05}^{0.09}$	$0.60_{0.48}^{0.12}$ $0.08_{0.06}^{0.12}$	$0.60_{0.46}^{0.19}$ $0.12_{0.08}^{0.19}$	$0.49_{0.34}^{0.26}$ $0.17_{0.12}^{0.26}$		$0.29_{0.19}^{0.19}$ $0.58_{0.36}^{0.80}$	$0.24_{0.14}^{0.02}$ $0.82_{0.71}^{1.02}$	$0.27_{0.16}^{0.42} \ 0.78_{0.63}^{0.94}$	$0.37_{0.24}^{0.51}$	$0.43_{0.29}^{0.39}$ $0.20_{0.14}^{0.33}$	$0.45_{0.29}^{0.13}$ $0.09_{0.07}^{0.13}$	$0.53_{0.39}^{0.65}$
YBG	0.07 0.05	0.080.06	$0.12_{0.08}$	0.170.12	$0.29_{0.20}^{0.43}$	0.580.36	0.620.71	0.780.63	$0.63_{0.45}^{0.78}$	0.200.14	$0.09_{0.07}$	$0.07_{0.06}^{0.09}$

Note. Sub/superscripts are 25th / 75th percentiles, respectively.

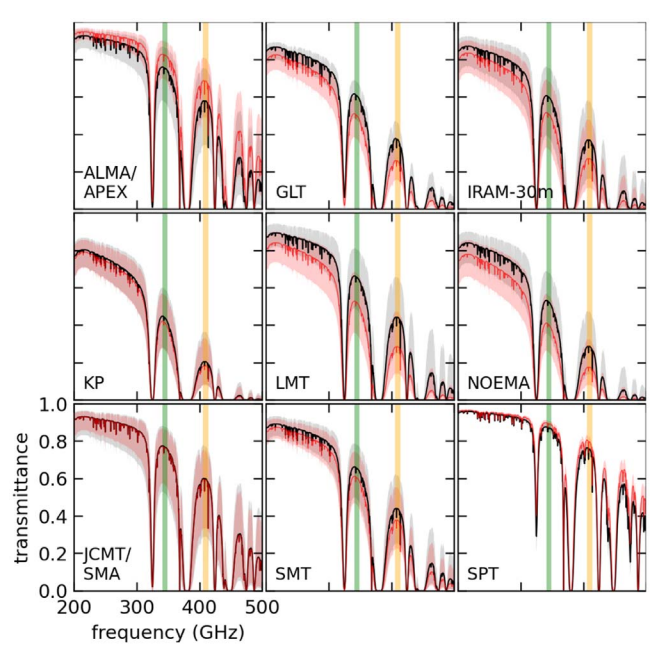


Figure 8. Zenith transmittance spectra at 200–500 GHz for existing EHT sites in March (black) and April (red). The shaded region brackets the interquartile range, and 8 GHz-wide high-frequency bands centered at 345 (green) and 410 GHz (yellow) are marked with vertical lines.

3.3. Improved Sampling of Fourier Components

The 230 GHz Fourier coverage for each candidate new site is plotted in Figure 10 for M87* and in Figure 11 for Sgr A*. These coverages are based on the source position and array geometry; we have not flagged low S/N visibilities as we do in the subsequent Monte Carlo filling-factor calculations. The coverage is for a full 24 hr of observing including times when ALMA cannot observe the source. Tracks corresponding to baselines with ALMA are plotted in bold. The tracks of the 2021 EHT array are underlaid in gray for reference. The 2021 array with ALMA lacks coverage between about 4 and 7 G λ in the north-south direction for both M87* and Sgr A*. Sgr A* also lacks mid-baseline coverage between 1 and 3 G λ as well as long-baseline coverage in the east-west direction. In these plots, an elevation cutoff of 10° was specified, which is especially important for the very short tracks at large u-v spacing, e.g., for FUJI and SPX toward M87*.

The number of new baselines is determined by the covisibility of the new site with the 2021 array with ALMA. For M87*, all of the considered sites that can observe that source form at least five new baselines. For Sgr A*, some sites form as few as two new baselines. The mean longitude of the 2021 EHT sites is 76° west. Sites near that longitude have significant covisibility with the existing EHT sites and with ALMA and therefore tend to make long u-v tracks.

Some site locations are more desirable than others because they sample obvious gaps in Fourier coverage. For M87*, the BOL, BRZ, CNI, BMAC, GAM, HAY, NZ, and YAN locations fill portions of the 4-7 G λ gap in the north–south direction. The BMAC, CAS, CAT, GAM, GARS, NZ, SGO, and YBG sites extend the longest baselines. For Sgr A*, the 2021 coverage contains gaps between 4 and 7 G λ in the north–south direction, which are filled by CAS, CAT, GARS, KEN, and KILI. Sites in central and southern Africa, e.g., KILI

together with GAM, could significantly improve the resolution of the array in the east—west direction.

The geometric Fourier coverage contributed by a new site is important, but only if the weather conditions at that new site are adequate for making detections. The Monte Carlo incremental coverage, which flags intervals with low S/N values based on the probabilistic weather at each site, is presented in Figure 12 for a specific set of observing parameters: 10 m antennas at new stations, simultaneous 230 and 345 GHz frequency coverage, and 8 GHz bandwidth in each of two sidebands. For the simulations in Figures 12 and 13, the observing schedule is limited to times when ALMA can see the source, which is consistent with previous EHT schedules (Event Horizon Telescope Collaboration et al. 2019c). The bandwidth per frequency band is a projected doubling of the present-day EHT (Event Horizon Telescope Collaboration et al. 2019a) and helps compensate for some of the additional noise at 345 GHz. For M87*, an extended 500 μ as FoV is specified, which is motivated by future efforts to connect horizon-scale structure with the M87* jet (Blackburn et al. 2019). For Sgr A*, a 150 μ as FoV is used. We assume an observing time commensurate with the variability timescale of each source. M87* evolves slowly, so a full observation is specified to maximize the coverage on each baseline. Sgr A* evolves on a timescale of minutes (Event Horizon Telescope Collaboration et al. 2019a), so a 100 s snapshot observation is simulated, which truncates the Fourier coverage. Our approach to flagging low S/N scans accounts for the noise contributed by the physical temperature of the atmosphere. This is important at low-altitude polar sites like GLT and GARS, where the cold atmosphere compensates for marginal opacity.

The Monte Carlo incremental filling factor is calculated in the following way. For the full observations, we report the Fourier filling of the augmented and fiducial arrays using the entirety of the Fourier coverage tracks, $F_{\rm aug}/F_{\rm fid}-1$. For the snapshot observations of Sgr A*, we vary the start time for the fiducial and augmented arrays independently to maximize the filling in each case: $\max{(F_{\rm aug})}/\max{(F_{\rm fid})}-1$. Depending on the coordinates of a new site, there might be no start times that produce greater snapshot Fourier filling than the fiducial array, which would make the incremental filling for that site zero. The maximum filling metric is a proxy for the best instantaneous coverage achievable by a new site.

The sites with the greatest incremental filling are added sequentially to the fiducial array as indicated beginning with the 2021 EHT sites. For M87*, SGO emerges as the site that adds the greatest Fourier coverage to the 2021 array with ALMA. Repeating the calculation for a 12 station array consisting of the 2021 EHT+SGO, CNI emerges as the next best site for increasing the Fourier coverage. Similarly for Sgr A* with a full observation, Dome A, KEN, BMAC, and Dome C yield the most incremental coverage. For Sgr A* with snapshot coverage, NZ adds the most coverage to the 2021 array, followed by Dome C, then CAT, and GARS. In general, the incremental coverage for a particular new site decreases as new sites are added to the fiducial array because there are fewer gaps in the Fourier coverage to fill. Our approach of adding the best locations in sequence makes the problem of selecting a group of sites computationally manageable and leads us to an array with excellent coverage. As the ngEHT develops, a comprehensive search for the

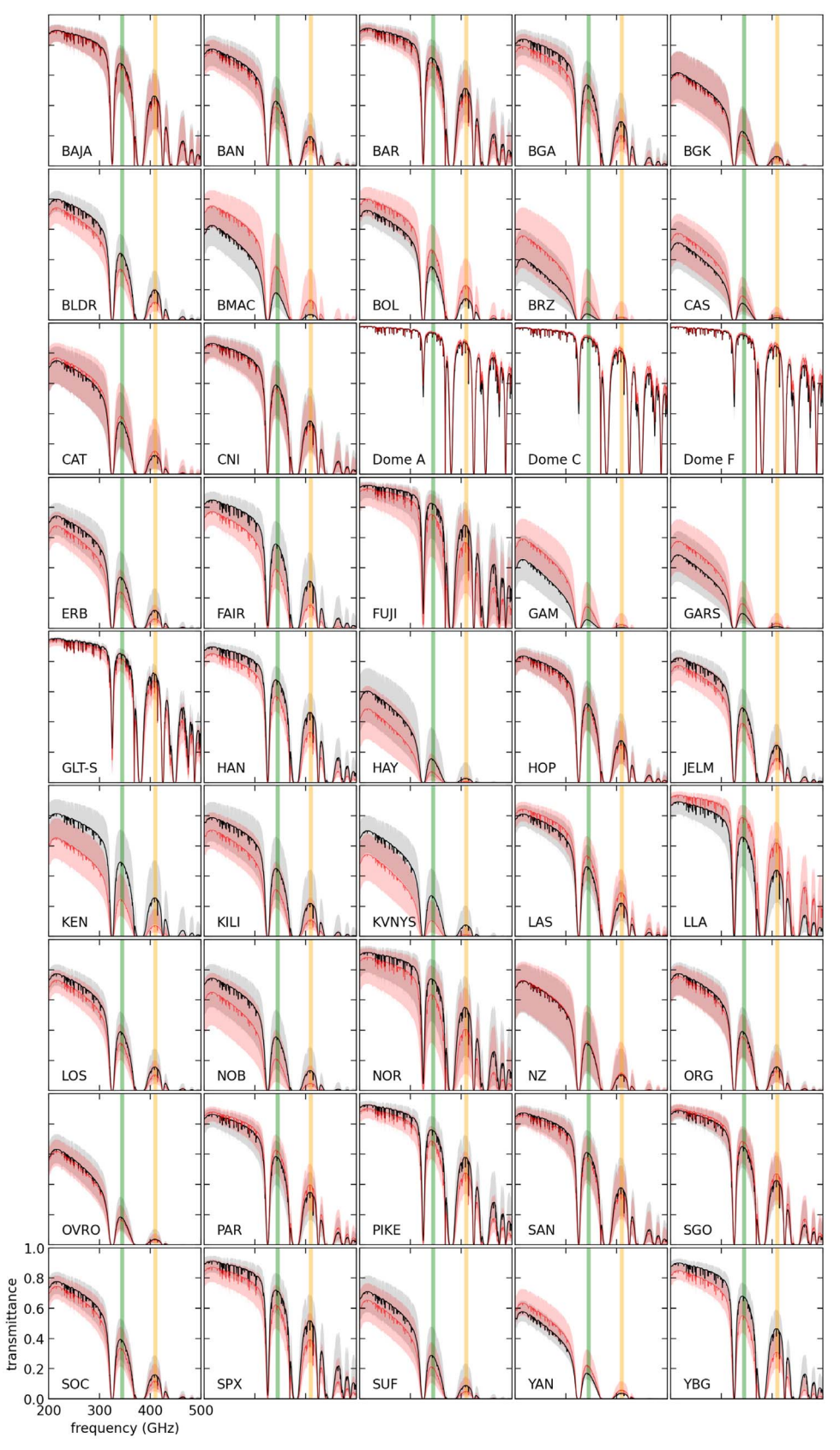


Figure 9. Zenith transmittance spectra at 200–500 GHz for candidate new EHT sites for March (black) and April (red). Shaded spectra are the interquartile range, and high-frequency 8 GHz-wide high-frequency bands centered at 345 and 410 GHz are marked with vertical lines.

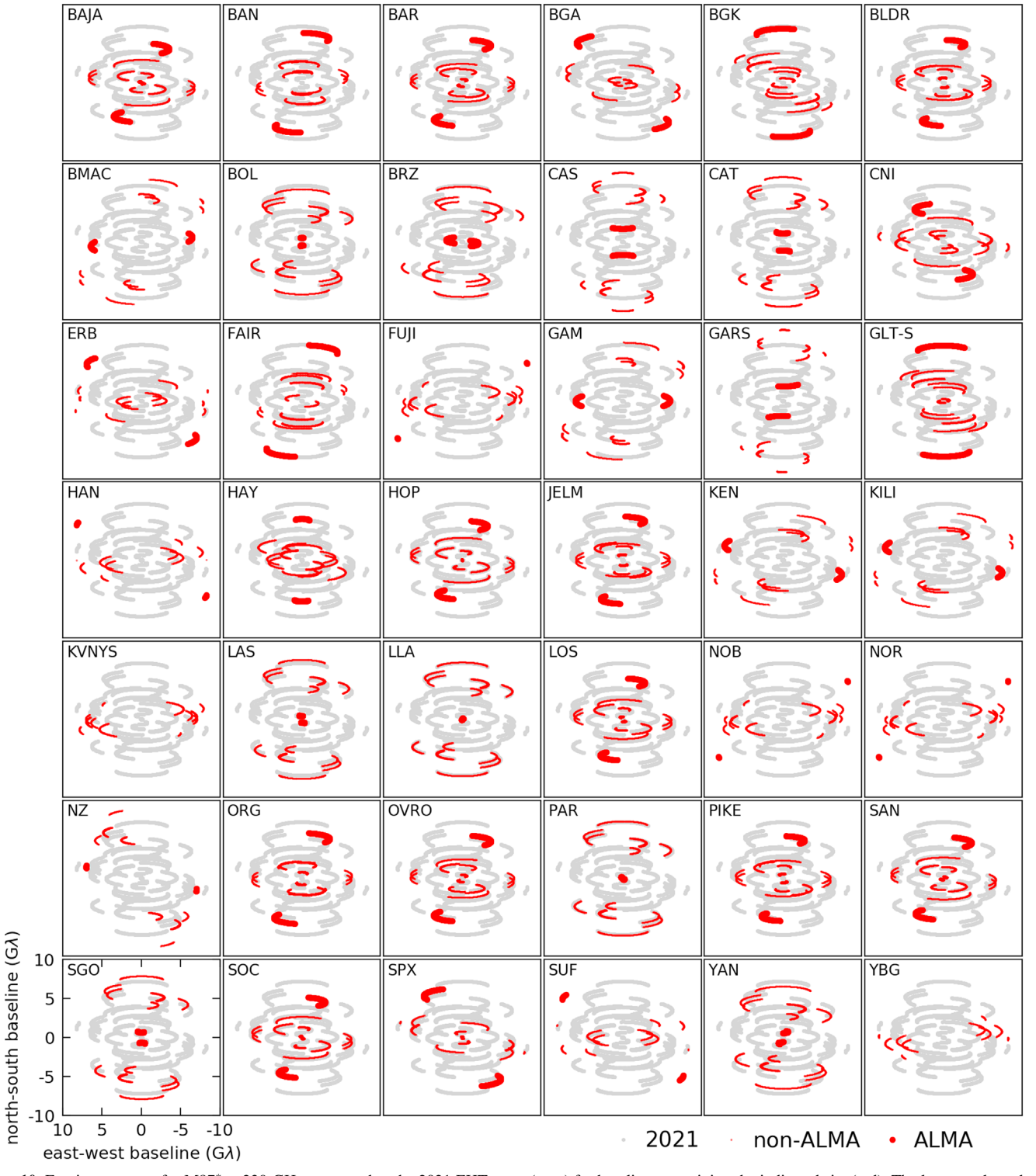


Figure 10. Fourier coverage for M87* at 230 GHz compared to the 2021 EHT array (gray) for baselines containing the indicated site (red). The large markers denote baselines to ALMA. Sidebands are omitted for clarity.

global optimum array could lead to a different selection of sites.

The Fourier filling factor we present here is one metric for approaching VLBI array design. While we favor the filling metric for its simplicity, other considerations and metrics could prioritize a different set of new sites and should be vetted in future design efforts.

3.4. Imaging with an Expanded Array

To demonstrate the improvement of horizon-scale imaging that would be possible with an expanded array under realistic meteorological conditions, we compare reconstructions made using the 2017, 2021, and an example ngEHT array. In the 2017 and 2021 arrays, we combine multiple 2 GHz-wide



Figure 11. Fourier coverage for Sgr A* at 230 GHz compared to the 2021 EHT array (gray) for baselines containing the indicated site (blue). The large markers denote baselines to ALMA. Sidebands are omitted for clarity.

fringe-finding bands for an aggregate bandwidth over two polarizations of 16 GHz in 2017 and 32 GHz in 2021. For the ngEHT array, we assume the same parameters as the filling factor calculation: dual-frequency 230 and 345 GHz observing

north-south baseline (Gλ)

with an aggregate bandwidth of 128 GHz over two polarizations. The bandwidth of the EHT backend has increased at regular intervals (Doeleman et al. 2008; Fish et al. 2011; Doeleman et al. 2012; Johnson et al. 2015; Event Horizon

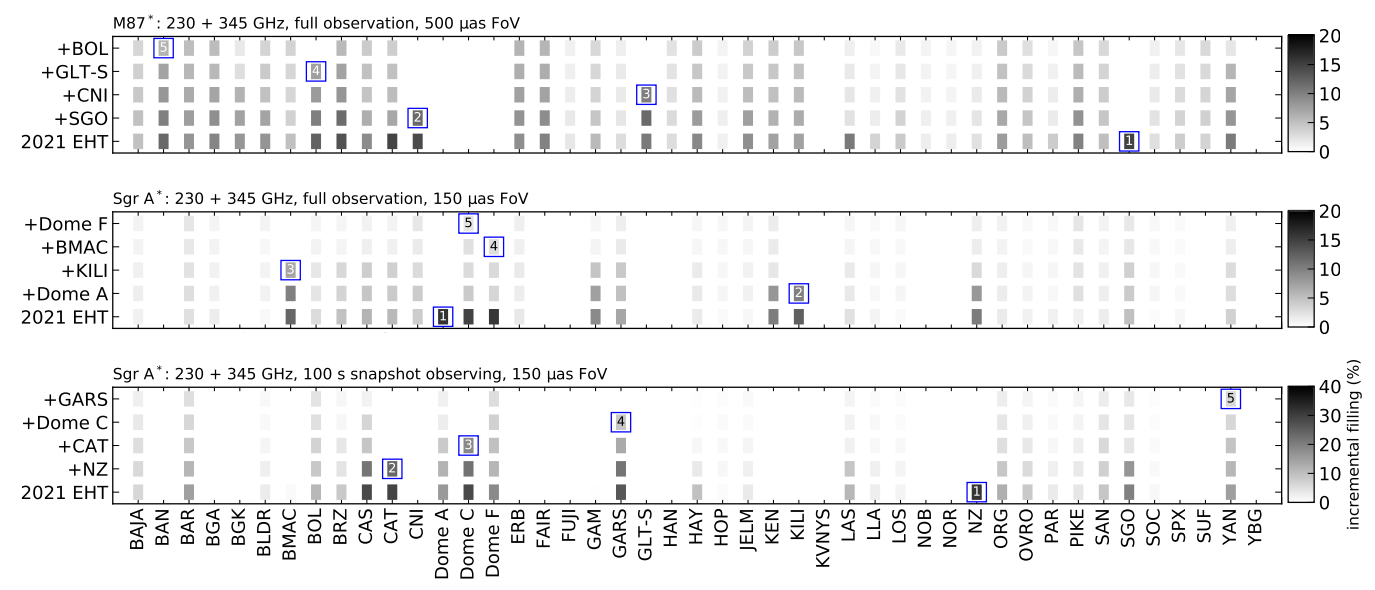


Figure 12. Incremental filling highlighting the sites with the best performance as the array grows incrementally. The simulated observations use April probabilistic meteorological conditions, and the filling reported is the mean of the Monte Carlo instantiations. Beginning with the 2021 EHT array, the incremental filling is calculated for the addition of each new site. The fiducial array is then augmented by the new site with the greatest incremental filling and the calculation is repeated again. For M87* (top panel), the 2021 coverage is improved most by SGO(1) followed by SGO+CNI(2) then by SGO+CNI+GLT-S(3), and so on. The same procedure was done for Sgr A* with a full observation (middle), and Sgr A* with a 100 s snapshot observation (bottom). The Sgr A* snapshot observing performance assumed to be simultaneous dual-frequency 230 + 345 GHz with 10 m antennas at new stations and an 8 GHz fringe-finding bandwidth in each of two sidebands. The M87* fractions are calculated assuming a 500 μ as FoV to encompass the base of the forward jet while the Sgr A* fractions assume a 150 μ as FoV. Snapshot fill fractions of zero have no more coverage than the fiducial array.

Telescope Collaboration et al. 2019a), and it is reasonable to anticipate continued improvement on the timescale of array expansion (Blackburn et al. 2019). The image reconstructions are shown in Figure 13. The thermal noise used for these reconstructions are calculated under median conditions.

For M87*, the FoV is extended and the temperature scale is logarithmic to highlight the base of the low-brightness forward jet. For this particular source model with the 2017 and 2021 arrays, the jet base is not faithfully reconstructed. In contrast, the additional stations in the ngEHT array and the addition of the 345 GHz band reproduces the jet out to more than five shadow diameters, and the diffuse flux surrounding the jet is more tightly constrained. The sites in the ngEHT panel were primarily chosen based on the leading sites from the Monte Carlo incremental filling analysis in Figure 12: three or four sites each for M87* and snapshot Sgr A*. BAJA, GAM, LLA, OVRO, and NOR were also included either because they sample interesting Fourier components or because they have significant infrastructure already in place. The ngEHT Fourier coverage on M87* extends to approximately 12 G λ under nominal meteorological conditions.

The Sgr A* reconstruction is shown in linear scale. We select a start time for the Sgr A* simulated observation when the Fourier filling is greatest. With 100 s snapshot observing, the Fourier tracks normally obtained through Earth-aperture synthesis become points. For the 2017 and 2021 arrays, the Fourier points are sparse, and the arrays and eht-imaging algorithms do not converge on the known structure; however, the large number of baselines in the ngEHT simulation fills a significant fraction of the Fourier plane even in snapshot mode.

The ngEHT is capable of reconstructing the ring emission of Sgr A* including the morphology of the discontinuity in the left-hand site of the image. A full multifrequency reconstruction with scattering mitigation is an active research topic; however, these short-timescale reconstructions suggest that detailed moviemaking of dynamical features at Sgr A* could be possible with the ngEHT.

4. Conclusions

We have evaluated potential new sites for the ngEHT and examined how they improve the capability of the EHT array to study M87* and Sgr A* in increasing detail. We have used meteorological statistics derived from the MERRA-2 reanalysis to develop a list of 45 potential new sites. Our site water vapor reanalyses of meteorological data are in close agreement with available in situ measurements. We find that a number of the candidate sites have, first, good conditions for submillimeter observations and, second, also sample new spatial frequencies on both large and small angular scales, which significantly enhances imaging fidelity of the EHT array. The Monte Carlo incremental filling calculation suggests that the priority sites strongly depend on details like the source and the FoV. Future work is planned for assessing the best array across a range of science cases and metrics; however, our example imaging reconstruction shows that under realistic median meteorological conditions, additional stations in the ngEHT will improve the ability to image lowflux, dynamical features for M87* and Sgr A*. Future work will also include field measurements over at least a full seasonal cycle to validate MERRA-2 against local conditions.

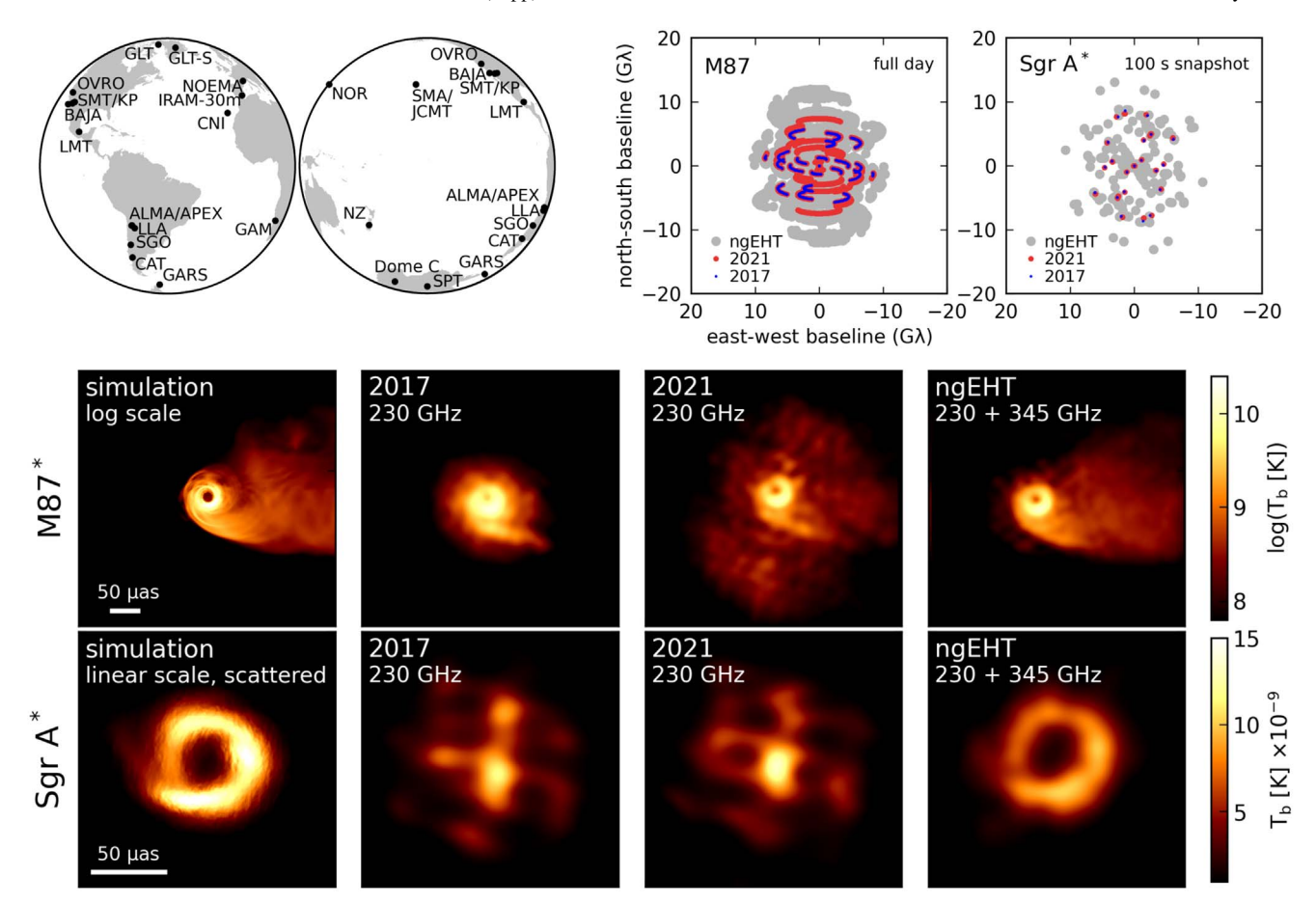


Figure 13. Imaging reconstructions of GRMHD simulations for M87* (from Chael et al. 2019, plotted in logarithmic scale flux density) and Sgr A* (from Chael et al. 2018, plotted in linear scale flux density). The simulation panels show the combined 230 and 345 GHz flux distributions where the high-frequency band has been scaled to the lower one using a spectral index obtained from the source model. We show Sgr A* as it would appear on the sky, scattered by the interstellar medium (Johnson 2016). Using SEFDs calculated in this meteorological study under median conditions for April, the 2017 and 2021 arrays are unable to reconstruct much of the forward-propagating jet in the M87* model or reconstruct the Sgr A* brightness distribution with a 100 s snapshot observation. The ngEHT reconstructions use the array shown on the globe, which augments the 2021 EHT with the leading sites based on the filling factor calculation in Figure 12 plus sites that have good existing infrastructure (BAJA, CAT, CNI, Dome C, GAM, GARS, GLT-S, LLA, NOR, NZ, OVRO, and SGO). The ngEHT reconstruction assumes a 10 m antenna diameter for new stations and an 8 GHz bandwidth per sideband. The 230 and 345 GHz bands are combined in the ngEHT reconstructions using the spectral indices. The ngEHT dramatically improves the Fourier coverage and reconstructions, both for M87* and for Sgr A* in snapshot mode.

We thank several members of the EHT Collaboration and T. K. Sridharan for suggesting potential new sites for study, Simon Radford for useful discussions about the SMA opacity logs, Andrew Chael for providing GRMHD source models. Antonio Fuentes whose MPI parallelization framework we adapted for the fill fraction calculations, Dom Pesce and Greg Lindahl for their assistance with the filling fraction code, and Sara Issaoun, Mareki Honma, Lynn Matthews, and Peter Galison for their useful feedback on the manuscript. We acknowledge the significance that Maunakea, where the SMA and JCMT EHT stations are located, has for the Hawaiian people. This work was supported in part by the National Science Foundation (AST-1935980, AST-1716536, OISE-1743747), the Gordon and Betty Moore Foundation (GBMF-5278), and the Black Hole Initiative at Harvard University, through a grant (60477) from the John Templeton Foundation.

ORCID iDs

Alexander W. Raymond https://orcid.org/0000-0002-5779-4767

Daniel Palumbo https://orcid.org/0000-0002-7179-3816 Scott N. Paine https://orcid.org/0000-0003-4622-5857 Lindy Blackburn https://orcid.org/0000-0002-9030-642X Rodrigo Córdova Rosado https://orcid.org/0000-0002-7967-7676

Sheperd S. Doeleman https://orcid.org/0000-0002-9031-0904

Joseph R. Farah https://orcid.org/0000-0003-4914-5625 Michael D. Johnson https://orcid.org/0000-0002-4120-3029 Freek Roelofs https://orcid.org/0000-0001-5461-3687 Remo P. J. Tilanus https://orcid.org/0000-0002-6514-553X Jonathan Weintroub https://orcid.org/0000-0002-4603-5204

References

Ananthasubramanian, P. G., Yamamoto, S., & Prabhu, T. P. 2002, IJIMW, 23, 227

Blackburn, L., Doeleman, S., Dexter, J., et al. 2019, arXiv:1909.01411
Blackburn, L., Pesce, D. W., Johnson, M. D., et al. 2020, ApJ, 894, 31
Booth, R. S., Delgado, G., Hagstrom, M., et al. 1989, A&A, 216, 315
Castro-Almazán, J. A., Muñoz-Tuñón, C., García-Lorenzo, B., et al. 2016, Proc. SPIE, 9910, 99100P

Chael, A., Narayan, R., & Johnson, M. D. 2019, MNRAS, 486, 2873Chael, A., Rowan, M., Narayan, R., Johnson, M., & Sironi, L. 2018, MNRAS, 478, 5209

Chael, A. A., Johnson, M. D., Bouman, K. L., et al. 2018, ApJ, 857, 23

```
Chael, A. A., Johnson, M. D., Narayan, R., et al. 2016, ApJ, 829, 11
Chamberlin, R. A. 2001, JGR, 106, 20101
Doeleman, S., Agol, E., Backer, D., et al. 2009, arXiv:0906.3899
Doeleman, S. S., Fish, V. L., Schenck, D. E., et al. 2012, Sci, 338, 355
Doeleman, S. S., Weintroub, J., Rogers, A. E. E., et al. 2008, Natur, 455, 78
Event Horizon Telescope Collaboration, Akiyama, K., Alberdi, A., et al.
   2019a, ApJL, 875, L2
Event Horizon Telescope Collaboration, Akiyama, K., Alberdi, A., et al.
   2019b, ApJL, 875, L1
Event Horizon Telescope Collaboration, Akiyama, K., Alberdi, A., et al.
   2019c, ApJL, 875, L3
Event Horizon Telescope Collaboration, Akiyama, K., Alberdi, A., et al.
   2019d, ApJL, 875, L4
Ferrusca, D., & Contreras, R. J. 2014, Proc. SPIE, 9147, 914730
Fish, V. L., Doeleman, S. S., Beaudoin, C., et al. 2011, ApJL, 727, L36
Gelaro, R., McCarty, W., Suárez, M. J., et al. 2017, JCli, 30, 5419
Graham, E., Vaughan, R., Buckley, D. A., & Tirima, K. 2016, ThApC,
   124, 425
Grasdalen, G. L., Gehrz, R. D., Hackwell, J. A., & Freedman, R. 1985, PASP,
   97, 1013
Ishiguro, M., Tanaka, H., Morita, K.-I., et al. 1986, in 1986 Antennas and
   Propagation Society Int. Symp. (Piscataway, NJ: IEEE), 531
Johnson, M. D. 2016, ApJ, 833, 74
Johnson, M. D., Fish, V. L., Doeleman, S. S., et al. 2015, Sci, 350, 1242
Johnson, M. D., Narayan, R., Psaltis, D., et al. 2018, ApJ, 865, 104
Kerber, F., Querel, R. R., & Neureiter, B. 2015, JPhCS, 595, 012017
Kimura, K., Aton, K., Baybayan, K., et al. 2019, BAAS, 51, 135
Lee, S.-S., Byun, D.-Y., Oh, C. S., et al. 2011, PASP, 123, 1398
Matsushita, S., Asada, K., Martin-Cocher, P. L., et al. 2017, PASP, 129,
```

025001

```
Marvil, J., Ansmann, M., Childers, J., et al. 2006, NewA, 11, 218
Matsushita, S., & Matsuo, H. 2003, PASJ, 55, 325
Paine, S. 2018, BH PIRE Winter School 2018 tutorial: Radio Climatology,
  https://bhpire.arizona.edu/education/tutorials/
Paine, S. 2019, The am atmospheric model, v11.0, Zenodo, doi:10.5281/
  zenodo.3406496
Palumbo, D. C. M., Doeleman, S. S., Johnson, M. D., Bouman, K. L., &
  Chael, A. A. 2019, ApJ, 881, 62
Pearson, T. J., & Readhead, A. C. S. 1984, ARA&A, 22, 97
Querel, R. R., Kerber, F., Lo Curto, G., et al. 2010, Proc. SPIE, 7733, 773349
Quesada, J. A. 1989, PASP, 101, 441
Radford, S. J. E., & Peterson, J. B. 2016, PASP, 128, 075001
Ricaud, P., Grigioni, P., Zbinden, R., et al. 2015, AntSc, 27, 598
Roelofs, F., Janssen, M., Natarajan, I., et al. 2020, A&A, 636, A5
Rogers, A., Barvainis, R., Charpentier, P., & Corey, B. 1993, ITAP, 41, 77
Rowan, M. E., Sironi, L., & Narayan, R. 2017, ApJ, 850, 29
Sault, R. J., & Wieringa, M. H. 1994, A&AS, 108, 585
Sekimoto, Y., Arikawa, Y., Aso, Y., et al. 2000, Proc. SPIE, 4015, 185
Sekimoto, Y., Yoshida, H., Hirota, T., et al. 1996, IJIMW, 17, 1263
Suen, J. Y., Fang, M. T., Denny, S. P., & Lubin, P. M. 2015, ITTST, 5, 299
Suen, J. Y., Fang, M. T., & Lubin, P. M. 2014, ITTST, 4, 86
Thompson, A. R., Moran, J. M., & Swenson, G. W. 2017, Interferometry and
  Synthesis in Radio Astronomy, Astronomy and Astrophysics Library (3rd
  ed.; Cham: Springer)
Tremblin, P., Schneider, N., Minier, V., Durand, G. A., & Urban, J. 2012,
    A&A, 548, A65
Usoff, J. M., Clarke, M. T., Liu, C., & Silver, M. J. 2014, LLabJ, 21, 83,
  https://www.ll.mit.edu/sites/default/files/page/doc/2018-05/21_1_6_
Wallace, L., & Livingston, W. 1984, PASP, 96, 182
```